Advances in single crystals and thin films of chiral hybrid metal halides

Zhihang Guo [a], Junzi Li [a], Rui Chen [b], Tingchao He [a,*]

[a] Key Laboratory of Optoelectronic Devices and Systems of Ministry of Education and Guangdong Province, College of Physics and Optoelectronic Engineering, Shenzhen University, Shenzhen, 518060, China
[b] Department of Electrical and Electronic Engineering, Southern University of Science and Technology, Shenzhen, 518055, China

ARTICLE INFO

ABSTRACT

Chiral organic–inorganic hybrid metal halides (HMHs), as an emerging class of chiral semi-conductor materials, have attracted unparalleled interest from multi-purpose perspectives, as a result of their easily accessible solution-grown methods, plentiful chemical structure and composition, as well as unique and exciting optoelectronic properties. Recently, substantial progress has been made in the synthesis of chiral HMHs, spectroscopic characterization and fabrication of optoelectronic devices. Although several reviews about the chiroptical properties and applications of chiral HMHs have been published, the comprehensive summary of the basic structural frameworks, fundamental physics and strategies for the modulation of optical activity, which are vital for the design of chiral HMHs and development of relevant optoelectronic applications, are still insufficient. In this review, we summarize the research progress from fundamentals to applications for the single crystals and thin films of chiral HMHs that are conducive to the development of practical optoelectronic devices. First, diverse structural frameworks and synthetic methods of chiral HMHs are systematically summarized. Afterward, fundamental physics and strategies for the modulation of optical activity as well as their related optoelectronic applications are comprehensively reviewed. Finally, we put forward the current challenges in this rapidly evolving field and present an outlook on future prospects to further develop chiral HMHs for various applications.

1. Introduction

Chirality refers to a structure lack of S_n symmetry elements [1], such as mirror plane (σ or S_1) and inversion (i or S_2) symmetry. Chiral materials exist widely in nature from small amino acid molecules, to macromolecular proteins, and to macroscopic crystals. Owing to the existence of non-centrosymmetric structures, chiral materials tend to exhibit distinct characteristics, and the most typical ability is to rotate the polarization plane of linearly polarized light [2]. In recent years, chiral materials have attracted extensive attention from the research community in interdisciplinary fields of chemistry, physics, biology and medicine and have shown promising optoelectronic applications in biometric detection and sensing [3–7], chiral bioimaging [8–10], chiral photonics and electronics [11–20].

Organic–inorganic hybrid metal halides (HMHs) were first reported as light absorbents in solar cells by Kojima and colleagues [21]. Given the intriguing photovoltaic properties of HMHs, such as high absorption coefficient, long carrier diffusion length and reasonable carrier mobility [22], the power conversion efficiency of solar cells based on HMHs has reached 25.5% from the initial 3.81% [23].

Furthermore, HMHs are also considered as excellent luminescent materials widely applied in light-emitting devices due to the low non-radiative recombination efficiency, high color purity and tunable emission [24–27]. The single crystals and thin films of HMHs, which are facile to be synthesized via cheap solution processing and multiple choices of organic and inorganic precursors, exhibit numerous merits such as low trap-state density, high mobility and well-defined dimension [28,29]. The HMHs provide various opportunities for high-performance optoelectronic applications. Importantly, the bulky and interchangeable organic sites of HMHs provide various possibilities for adjusting structural and optoelectronic characteristics, which allows the incorporation of chiral organic molecules to extend their applications. Owing to the large variety of chiral molecules readily available via organic synthesis, the single crystals and thin films of chiral HMHs represent a very promising platform for regulating their chirality and facilitating future optoelectronic devices with high-performance.

To date, several reviews have presented the research progress in chiral HMHs and proposed some constructive views [30–34]. Nevertheless, there is still a lack of a comprehensive summary on the basic structural frameworks, fundamental physics and strategies for the modulation of optical activity of chiral HMHs, especially on their single crystals and thin films that are vital for practical optoelectronic application. Here, we present an in-depth review on the research progress in these aspects that have not been fully addressed in the existing reviews. It is also noteworthy that most previous reviews used the term "perovskites" to describe all kinds of organic–inorganic HMHs, although many of them are not strictly perovskite structures [35]. Instead, we adopt the generalized term "HMHs" to describe the materials discussed in this review. This review is divided into the following sections. First, we discuss the structural frameworks of chiral HMHs, including diverse dimensions, helical structures and heterostructures, as described in Section 2. Then, Section 3 will summarize various synthetic methods for the fabrication of single crystals and thin films of chiral HMHs. Fundamental physics and strategies for the modulation of optical activity will be introduced in Section 4, while the related optoelectronic applications of chiral HMHs will be systematically reviewed in Section 5. Finally, a brief summary and outlook on current challenges and future research opportunity of chiral HMHs will be presented in the last Section 6.

2. Structural frameworks

Several generic colloidal chemistry approaches, such as grafting chiral organic ligands onto semiconductor nanocrystals [11,36,37], direct synthesis using chiral molecular precursors [38–40] and chiral supramolecular self-assembly [41,42], have been developed to achieve optical activity of materials. However, HMHs allow the introduction of chiral molecules to directly induce participation in crystallization through easily accessible solution-grown techniques [43,44], which are more suitable for the commercialization of future optoelectronic devices. The timeline of research progress on chiral HMHs can be found in Fig. 1 and Table 1. In brief, the pioneered work on the synthesis of chiral HMHs was reported by Billing and Lemmerer in 2003 and 2006 by introducing chiral molecules into organic–inorganic HMHs [45,46]. After ten years of silence, until 2017, Moon et al. investigated the chiroptical behavior of chiral HMHs [47]. Chiral HMHs re-spring up and surprisingly arouse extensive research interest, and the exploration of related chiral optoelectronic properties and applications is rapidly expanding.

Among 230 types of crystallographic space groups, 11 pairs are chiral space groups and the inversion through a point in each pair will transform one space group into another [48]. Importantly, 65 types of space groups (known as Sohncke space groups) that contain symmetry operations of only the first kind (*i.e.*, rotations and translations) can exhibit chirality as a result of their chiral crystal structures [49], comprising 43 types of space groups in achiral space groups and 22 types of chiral space groups (Fig. 2). What is often overlooked is that there are only 22 types of chiral space groups, while the other 43 types of Sohncke space groups cannot be called that way [48]. In addition, it has long been established theoretically that the crystals with four types of achiral crystal structures can also produce optical activity, including point groups C_s, C_{2v}, S_4, and D_{2d} [48,50,51]. The crystallographic relationship between physical properties and non-centrosymmetric crystal categories is summarized in Fig. 3 [52]. Interestingly, the variable crystal structure and composition of the chiral HMHs provide great convenience for adjusting their optoelectronic properties. So far, diverse dimensions at the molecular level, such as three-dimensional (3D) network, two-dimensional (2D) layer, one-dimensional (1D) chain and zero-dimensional (0D) isolated structure, have been demonstrated in chiral HMHs. In addition, optical activity has also been observed in the HMHs with helical structures and heterostructures.
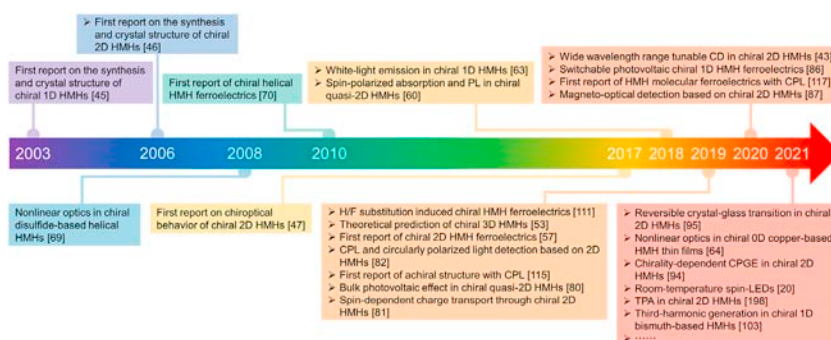

Fig. 1. Research timeline of the optoelectronic properties and pioneering discoveries in the development of chiral HMHs.

Table 1

Summary of chiral HMHs reported in the literature.

Year	Chemical Formula	Morphology	Structure	Highlights	Ref.
2003	(S-MBA)PbBr$_3^a$	Crystals	1D	Crystal structure	[45]
2006	(R-MBA)PbX$_3$ (X = Cl and Br)^a	Crystals	1D, 2D	Crystal structures	[46]
	(R-/S-MBA)PbI$_3^a$				
	(R-/S-MBA)$_2$PbI$_4^a$				
	α-(H$_3$N(CH$_2$)$_2$S–S(CH$_2$)$_2$NH$_3$)PbI$_5$·H$_3$O	Crystals	Helix	Reversible solid-state transition, switchable SHG	[68]
2008	α-(H$_3$N(CH$_2$)$_2$S–S(CH$_2$)$_2$NH$_3$)BiI$_5$	Crystals	Helix	Structural transformation, NLO properties	[69]
2010	(m-RBz-1-APy)PbI$_3^b$	Crystals	1D helix	Crystal structures, ferroelectrics	[70]
2013	(R-/S-CHEA)$_8$Pb$_3$I$_{14}^c$	Crystals	1D, 2D	Crystal structures	[78]
	(R-/S-CHEA)PbBr$_3^c$				
	(R-/S-CHEA)$_2$PbCl$_4^c$				
2015	(R-1-NEA)$_2$CuCl$_4^d$	Crystals	0D	Crystal structures, thermochromic behavior, PL	[109]
	(R-2-NEA)$_2$CuCl$_4^e$				
	(R-/S-CPEA)$_3$CoCl$_5^f$	Crystals	1D helix	Crystal structures	[108]
2016	(R-/S-MBA)$_2$CuCl$_4^a$	Crystals	0D	Crystal structures, biological activities	[79]
2017	(R-/S-MBA)$_2$PbI$_4^a$	Crystals, films	2D	CD, synthetic conditions	[47]
2018	(R-APD)PbCl$_4$·H$_2$O^g	Crystals	1D	White-light emission, SHG, CD	[63]
	(R-/S-MPEA)$_{1.5}$PbBr$_{3.5}$(DMSO)$_{0.5}^h$	Crystals, films, nanowires	2D	CD (films), PL, SHG (nanowires)	[130]
	N.A.	Films	Quasi-2D	CD, photophysical properties, spin-polarized absorption and PL	[60]
	(R-/S-MBA)$_4$Bi$_2$Br$_{10}^a$	Crystals, films	2D	Crystal structures, CD, SHG	[110]
2019	(R-/S-1-NEA)$_2$Pb$_4$Cl$_{10}$·2DMF^d	Crystals	2D	Crystal structures, PL	[116]
	(R-AQ)CuX$_4$ (X = Cl and Br)^i	Crystals	0D	Phase transition behavior, SHG	[112]
	(R-/S-FP)MnCl$_3^j$	Crystals	1D	H/F substitution, vibrational CD, ferroelectrics	[111]
	(R-/S-CFMA)PbI$_3^k$	N.A.	3D	Theoretical prediction of 3D chiral HMHs	[53]
	(R-/S-CPEA)$_2$PbI$_4^c$	Crystals	2D	Vibrational CD, ferroelectrics, PL	[57]
	(R-/S-MBA)$_2$PbI$_4^a$	Crystals, films	2D	CD, temperature-dependent CPL, circularly polarized light detection	[82]
	(R-/S-APD)PbBr$_3^g$	Crystals	1D helix	SHG, CD, PL	[83]
	(R-/S-MBA)PbI$_3^a$	Crystals, films	1D	CD, the origin of CD, flexible circularly polarized light detection	[62]
	(R-/S-FP)CdCl$_3^j$	Crystals, films	1D	H/F substitution, vibrational CD, ferroelectrics	[114]
	(R-/S-MBA)$_2$PbI$_4^a$	Crystals, films	2D	Room-temperature synthesis, CD, CPL, circularly polarized light detection	[131]
	(R-/S-HPD)CdCl$_3^l$	Crystals	1D helix	Room-temperature stable α and β forms, phase transition behavior, SHG	[113]
	(KC)$_2$MnX$_4$ (X = Cl and Br)^m	Crystals	0D	Achiral single crystals, CPL	[115]
	(R-/S-MPEA)$_2$(MA)Pb$_2$I$_7^h$	Crystals	Quasi-2D	Crystal structures, bulk photovoltaic effect	[80]
	(R-/S-MBA)$_2$PbI$_4^a$	Crystals, films	2D	CD, CISS, spin-dependent charge transport	[81]
2020	(R-/S-MBA)$_4$Cu$_4$I$_4^a$	Crystals	0D	Crystal structures, CPL, CD	[65]
	(R-/S-MPEA)$_2$(MA)Pb$_2$I$_7^h$	Crystals, films	Quasi-2D	CD, film crystallization dynamics, flexible circularly polarized light detection	[61]
	(R-/S-MBA)$_2$PbI$_{4(1-x)}$Br$_{4x}^a$	Films	2D	Tunable CD behavior	[43]
	(R-/S-2-NEA)$_2$PbI$_{4(1-y)}$Br$_{4y}^e$				
	(R-/S-MBA)$_2$PbI$_4^a$	Crystals, films	2D, 1D	Synthetic methods, CD, CPL ((R-/S-MBA)PbBr$_3$)	[84]
	(R-/S-MBA)PbX$_3$ (X = Br and I)^a				
	(R-/S-CHEA)PbI$_3^c$	Crystals, films	1D	Crystal structures, switchable ferroelectrics, CD	[86]
	(R-/S-FP)MnBr$_3^j$	Crystals	1D	Vibrational CD, ferroelectrics, CPL	[117]
	(R-/S-MPEA)$_2$PbBr$_4^h$	Crystals, films	2D	CD, white-light emission	[90]
	(R-/S-CTA)$_2$CuCl$_4^a$	Crystals, films	0D	Vibrational CD, CD, thermochromic ferroelastics, switchable physical properties	[123]
	(R-/S-FPEA)$_4$E$_2$X$_{10}$ (E = Sb and Bi; X = Cl, Br and I)^o	Crystals	2D	Crystal structures, optical properties, SHG	[85]
	PbBr$_2$:CsBr:(R-/S-1-NEA)Br^d	Films	Quasi-2D	CD, room-temperature CPL	[15]
	(HA)SbI$_5^p$	Crystals	1D	Crystal structures, semiconducting properties, photodetector	[89]
	(R-/S-MBA)$_2$SnI$_4^a$	Crystals, films	2D	Crystal structures, tunable CD, CISS	[44]
	(R-MPEA)$_2$CuX$_4$ (X = Cl and Br)^h	Crystals	2D	Thermal stability, phase transition behavior, dielectric responses	[118]
	(R-DMOA)$_2$CuX$_4$ (X = Cl and Br)^q				
	(R-DMOA)$_2$PbX$_4$ (X = Cl and Br)^q				
	(R-/S-MPEA)$_2$PbBr$_4^h$	Crystals, films	2D	Crystal structures, CD, white-light emission	[119]
	(R-/S-MBA)$_2$PbI$_4^a$	Crystals, films	2D	CISS, CD, magneto-optical detection	[87]
	(R-X-para-MBA)$_2$PbBr$_4$ (X = H, F, Cl and Br)^a	Crystals	2D	PL, CD, chirality transfer and amplification	[92]
	(R-/S-MPEA)$_2$CuCl$_4^h$	Crystals	2D	Crystal structures, CD, ferromagnets	[91]
	(R-/S-1-NEA)$_2$PbBr$_4^d$	Crystals, films	2D	CD, PL, Rashba-Dresselhaus SOC	[19]
	(R-/S-MBA)$_2$PbI$_4^a$	N.A.	2D	Theoretical proof of spin transport and chirality	[184]
	(R-/S-1-NEA)PbI$_3^d$	Films	1D helix,	Synthetic methods, CD, circularly polarized light detection	[71]
	(R-/S-1-NEA)$_2$PbI$_4^d$		2D		

(continued on next page)

Table 1 (*continued*)

Year	Chemical Formula	Morphology	Structure	Highlights	Ref.
2021	$(R\text{-}/S\text{-MBA})_2PbI_4^a$	Crystals, films	2D	CD, CISS (out-of-plane response), CPGE (in-plane response)	[96]
	$(R\text{-}/S\text{-HPD})CdCl_3^l$	Crystals	1D helix	Phase transition behavior, ferroelectrics	[121]
	$(R\text{-}/S\text{-MPEA})_4AgBiI_8^h$	Crystals, films	2D	CD, bulk photovoltaic effect, self-powered circularly polarized light detection	[88]
	$(R\text{-MPA})_2CdCl_4^r$	Crystals	2D, 1D	CD, SHG, switchable ferroelectrics	[66]
	$(R\text{-}/S\text{-}1\text{-NEA})_2PbBr_4^d$	Crystals	2D	Reversible crystal–glass transition	[95]
	$(R\text{-}/S\text{-MBA})_2CuCl_4^s$	Films	0D	CD, theoretical explanation of enhanced CD, SHG	[64]
	$(R\text{-}/S\text{-DMFP})CdCl_3^s$	Crystals	1D	H/F substitution, vibrational CD, dual-phase transition behavior	[120]
	$(R\text{-}/S\text{-BPEA})_2PbI_4^t$	Crystals, films	2D	CD, chirality-dependent CPGE	[94]
	$(R\text{-}/S\text{-MBA})_2PbI_4^a$	Crystals, films	2D	CD, CISS, spin-LEDs, spin dynamics	[20]
	$(R\text{-}/S\text{-PEDA})PbI_4^u$	Crystals, films	2D	Vibrational CD, ferroelastic ferroelectrics, reversible thermochromism	[97]
	$(R\text{-}/S\text{-MBA})_2CuCl_4^a$	Crystals, films	0D	CD, circularly polarized light detection	[93]
	$(R\text{-}/S\text{-MPEA})_2CuCl_4^h$	Crystals	2D	Ferromagnets, magneto-electric correlation	[126]
	$(R\text{-MP})PbX_3$ (X = Br and I)^v	Crystals	1D	Phase transition behavior, dual dielectric and NLO switches	[122]
	$(R\text{-HP})_2SbBr_5^w$ $(R\text{-HP})_5Sb_4Br_{17}^w$	Crystals	1D, 0D	Crystal structures, SHG, piezoelectrics $((R\text{-HP})_5Sb_4Br_{17})$	[124]
	$(PBA)_2CdCl_4^x$	Crystals	2D	Crystal structures, SHG, ferroelectrics	[175]
	$(R\text{-}/S\text{-APEA})_2PbI_4^y$	Crystals	2D	CD, CPL, PL with dual-stimuli-response to thermal and pressure	[125]
	$(R\text{-}/S\text{-AlaH})PbX_3 \cdot H_2O$ (X = Br and I)^z	Crystals	2D	Crystal structures, PL	[129]
	$(R\text{-}/S\text{-MPEA})_2SnBr_6^h$	Crystals, films	0D	Crystal structures, CD, phase transitions behavior, SHG	[127]
	$(R\text{-}/S\text{-APD})PbI_4^g$	Crystals	1D	Crystal structures, CD, chirality-dependent SHG	[101]
	$(R\text{-}/S\text{-MPEA})_2MAPb_2I_7/MAPbI_3^h$	Crystals	Quasi-2D/3D	Heterostructures, CD, circularly polarized light detection	[77]
	$(R\text{-}/S\text{-HP})_2RbBiBr_6^w$	Crystals	3D	Crystal structures, ferroelectrics, CPL	[54]
	$(R\text{-}/S\text{-X-MBA})_2PbI_4$ (X = H, F, Cl, Br and I)^a	Crystals, films	2D	Tunable CD and CPL intensities	[98]
	$(R\text{-}/S\text{-MBA})PbBr_3^a$	Crystals, films	1D	CD, CISS, spin-dependent charge transport	[99]
	$(R\text{-}/S\text{-MBA})_2CuX_4$ (X = Cl, and Br)^a	Crystals, films	0D	CD, CISS, spin-dependent charge transport	[128]
	$(R\text{-}/S\text{-BPEA})_2PbI_4^t$	Crystals	2D	CD, TPA, circularly polarized light detection	[100]
	$(R\text{-}/S\text{-CPEA})_2PbI_4^f$	Microwire arrays	2D	Single-crystalline microwire arrays, anisotropic SHG and TPA	[198]
	$(R\text{-}/S\text{-MPEA})_2PbCl_4/Si^h$	Crystals	2D	Heterostructures, CD, circularly polarized light detection in ultraviolet region	[164]
	$(R\text{-}/S\text{-MBA})BiI_4^a$	Crystals, films	1D	Crystal structures, CD, PL, SHG, third-harmonic generation	[103]
	$(R\text{-}/S\text{-MP})PbBr_3^v$	Crystals, films	1D	CD, SHG	[105]
	$(R\text{-}/S\text{-MPEA})(propylammonium)PbI_4^h$ $(R\text{-}/S\text{-MPEA})(butylammonium)PbI_4^h$	Crystals, films	2D	Crystal structures, alkyl–aryl mixing cation, tunable CD	[106]

Note: Abbreviations: ^{a}MBA: α-methylbenzylammonium; ^{b}m-RBz-1-APy$^+$: 3-RBenzylidene-1-aminopyridinium (R = NO$_2$, Br, Cl, or F); ^{c}CHEA: 1-cyclohexylethylammonium; ^{d}1-NEA: 1-(1-naphthyl)ethylammonium; ^{e}2-NEA: 1-(2-naphthyl)ethylammonium; ^{f}CPEA: 1-(4-chlorophenyl)ethylammonium; ^{g}APD: 3-aminopiperidinium; ^{h}MPEA: β-methylphenethylammonium; ^{i}AQ: aminoquinuclidinium; ^{j}FP: 3-fluoropyrrolidinium; ^{k}CFMA: chlorofluoromethylammonium; ^{l}HPD: 3-hydroxypiperidinium; ^{m}KC: [K(dibenzo-18-crown-6)]$^+$; ^{n}CTA: 3-chloro-2-hydroxypropyltrimethylammonium; ^{o}FPEA: 1-(4-fluoro)-phenylethylammonium; ^{p}HA: histaminium; ^{q}DMOA: 3,7-dimethyloctylammonium; ^{r}MPA: 1-methyl-3-phenylpropylammonium; ^{s}DMFP: *N,N*-dimethyl-3-fluoropyrrolidinium; ^{t}BPEA: 1-(4-bromophenyl)ethylammonium; ^{u}PEDA: *N*-(1-phenylethyl)ethane-1,2-diaminium; ^{v}MP: 2-methylpiperidinium; ^{w}HP: 3-hydroxypyrrolidinium; ^{x}PBA: 4-phenylbutylammonium; ^{y}APEA: (4-aminophenyl)ethylammonium; ^{z}Ala: α-alanine.

2.1. Dimensions

2.1.1. 3D structure

3D HMHs are defined as an infinite framework formed by small cations and corner-sharing inorganic metal halide units extending in all crystallographic directions. Compared with other low-dimensional HMHs, chiral 3D HMHs possess lower exciton binding energy and longer carrier diffusion lengths, suggesting they are more promising in the application of high-performance chiral optoelectronics and spintronics. However, the exploration of chiral 3D HMHs remains a challenge, in which small cations are required to fit into the void space between the octahedra and prevent the 3D crystal structure from being stretched to other dimensions. Choosing chiral cation as the organic component, Long et al. theoretically demonstrated that the introduction of chiral *R* or *S*-chlorofluoromethylammonium (*R*-/*S*-CFMA) cation can transfer the chirality of organic molecules to the internal structural framework and produce 3D HMHs (Fig. 4a) [53]. Based on theoretical calculation, the 3D (*R*-/*S*-CFMA)PbI$_3$ crystal structures were proven to be kinetically and thermodynamically stable. Importantly, the theoretically predicted chiral HMHs may exhibit various interesting properties, such as optical rotation, circular dichroism (CD), second harmonic generation (SHG), piezoelectricity, pyroelectricity, and ferroelectricity [53]. Very recently, Ye et al. reported the synthesis of chiral 3D bimetal halides with ferroelectricity and ferroelasticity, *i.e.*, (*R*-HP)$_2$RbBiBr$_6$ (*R*-HP = *R*-3-hydroxypyrrolidinium) [54]. Moreover, the chiral (*R*-/*S*-HP)$_2$RbBiBr$_6$ exhibited fascinating circularly polarized luminescence (CPL)
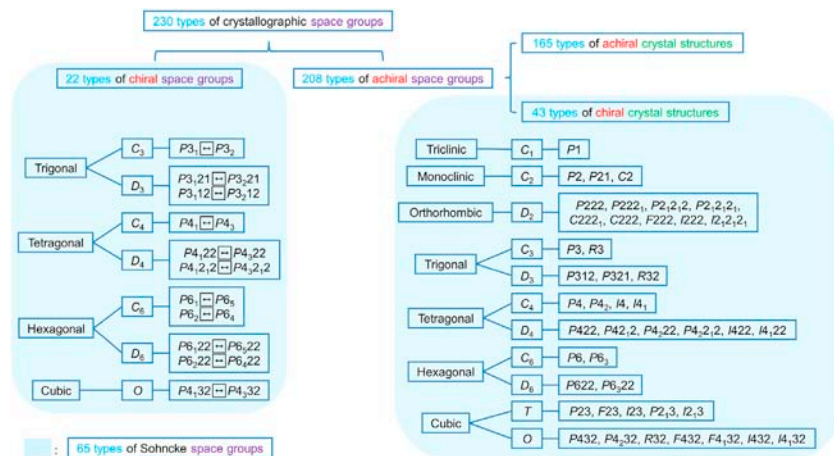
Fig. 2. Detailed classifications of 230 types of crystallographic space groups. The space groups and crystal structures of chiral or achiral are listed separately.
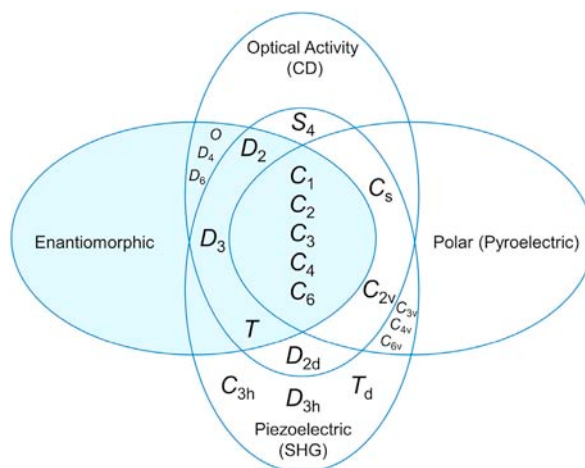

Fig. 3. Structure–property relationship of non-centrosymmetric crystals. Reproduced with permission from Ref. [52]: Copyright 1998, American Chemical Society.

and semiconducting properties.

2.1.2. 2D and quasi-2D structures

Typically, 2D and quasi-2D (also regarded as Ruddlesden–Popper-type) HMHs are characterized by corner-sharing inorganic metal halide units sandwiched between specific $\langle n \rangle$-layers of organic molecules. In particular, $\langle n \rangle = 1$ and ∞ stands for the cases of pure 2D and 3D HMHs, respectively, where $\langle n \rangle$ is the average number of inorganic metal halide monolayers separated by the bulky organic molecules [55]. In contrast to the strict restriction on small cations in the 3D structure, the pure 2D layered structure with a general formula $(RNH_3)_2BX_4$ or $(H_3NRNH_3)BX_4$ (R stands for bulky organic functional groups, B is a metal cation, and X is a halide anion) can accommodate larger and more complex organic cations [56]. As the most typical structures of chiral HMHs, work on the design and synthesis of chiral 2D HMHs is currently in full swing and significant progress has been made to date. By introducing the chiral enantiomer molecule, *i.e.*, *R*- or *S*-α-methylbenzylamine (*R-/S*-MBA), Moon et al. reported the synthesis and chiroptical properties of $(R-/S\text{-MBA})_2PbI_4$ thin films featuring 2D structural characteristics and crystallizing in space group $P2_12_12_1$ with chiral crystal structure (Fig. 4b) [46]. Also, Xiong et al. reported the 2D lead iodide ferroelectrics $(R-/S\text{-CPEA})_2PbI_4$ (*R-/S*-CPEA = *R-/S*-1-(4-chlorophenyl) ethylammonium) with outstanding ferroelectric performance and unique chirality [57].

It is worth noting that pure 2D HMHs usually exhibit poor photoluminescence (PL) at room temperature due to the barrier of inter-layer charge transfer caused by insulating organic molecules and fast nonradiative exciton quenching caused by strong exciton-phonon coupling within the layers [58,59]. Therefore, extensive exploration of quasi-2D HMHs has been performed. For example, Long et al. reported spin control in quasi-2D HMHs and both spin-polarized absorption and PL were observed in these quasi-2D HMHs in the absence of an external magnetic field [60]. In the category of crystal structures of quasi-2D HMHs, as depicted in Fig. 4c, the chirality of
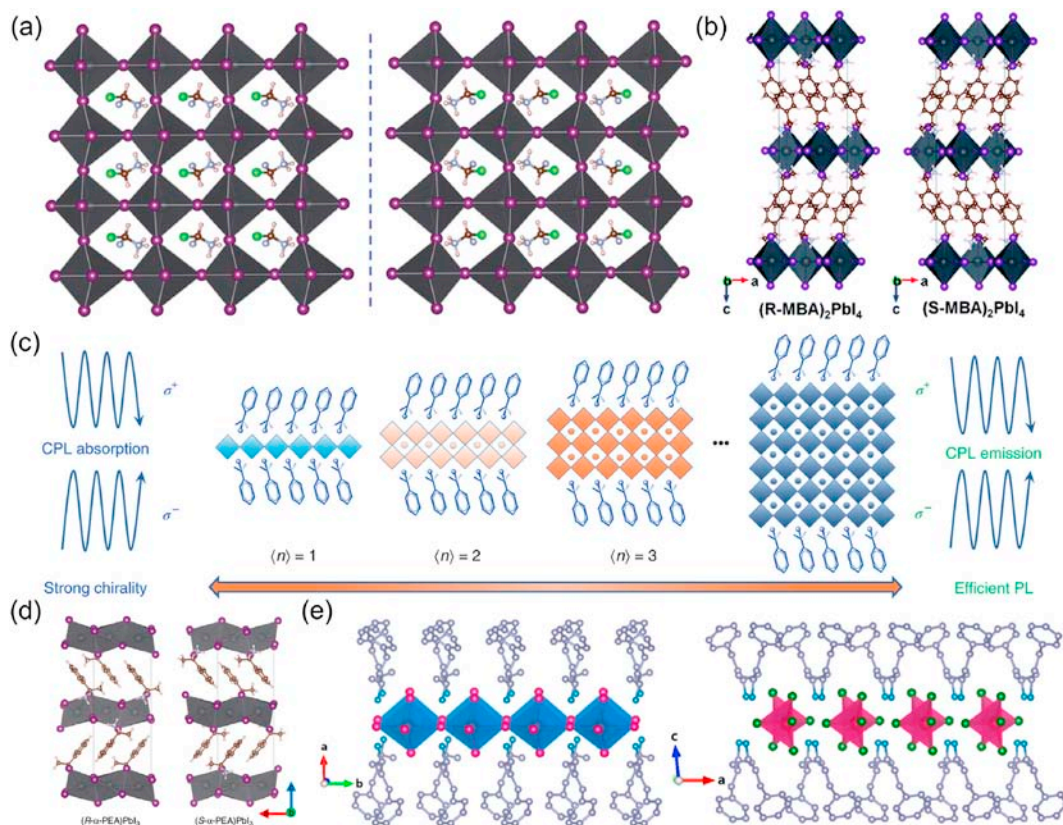
Fig. 4. Schematic illustration of chiral HMHs in diverse dimensions. (a) Optimized structures of 3D (*R-/S*-CFMA)PbI$_3$. Reproduced with permission from Ref. [53]: Copyright 2019, John Wiley and Sons. (b) Crystalline structures of 2D (*R-/S*-MBA)$_2$PbI$_4$. Reproduced with permission from Ref. [47]: Copyright 2017, Royal Society of Chemistry. (c) Schematic illustration of crystal structures of quasi-2D HMHs with different inorganic ⟨*n*⟩-layers. Reproduced with permission from Ref. [60]: Copyright 2018, Springer Nature. (d) Crystal structure of 1D (*R-/S*-MBA)PbI$_3$. Reproduced with permission from Ref. [62]: Copyright 2019, Springer Nature. (e) Crystal structures of 1D (left) and 0D (right) (*R*-MPA)$_2$CdCl$_4$ at room temperature viewed from the *c-* and *b*-axes, respectively. Reproduced with permission from Ref. [66]: Copyright 2021, American Chemical Society.

HMHs increases with the decrease of average number of inorganic metal halide monolayers. As a result, the pure 2D HMHs exhibit the strongest chirality [60]. Differently, quasi-2D crystal structures (⟨*n*⟩ = 2) endow HMHs with chirality and PL properties simultaneously, and the latter is achieved through efficient energy funnelling [60]. To explain whether the quasi-2D HMHs possess inherent chirality and the capability to distinguish different polarization states of photons, Wang et al. synthesized chiral quasi-2D HMHs for flexible circularly polarized light detection, in which the device responsivity is almost one order of magnitude higher compared with pure 2D HMHs [61].

2.1.3. 1D structure

In 1D HMHs, the inorganic metal halide units that share corner-, edge-, or face can form a 1D chain surrounded by organic cations. In 2003, Billing and Lemmerer pioneered to report the synthesis and crystal structure of 1D (*S*-MBA)PbBr$_3$ HMHs, which was another configuration templated by chiral organic molecule *S*-MBA [45]. Later, Tang et al. reported the chiroptical properties of 1D (*R-/S*-MBA) PbI$_3$ HMHs and applied them to fabricate circularly polarized light detectors [62]. As illustrated in Fig. 4d, the (*R-/S*-MBA)PbI$_3$ exhibits a 1D crystal structure consisting of extended face-sharing [PbI$_6$]$^{4-}$ octahedral chains, which are orientated along the *a*-axis and separated by isolated organic cations. It is worth mentioning that the anisotropy factor (*g*$_{abs}$) of the 1D (*R-/S*-MBA)PbI$_3$ is ~0.02, which is three times higher than that of 2D (*R-/S*-MBA)$_2$PbI$_4$. In addition, chiral 1D HMHs that exhibit white-light emission with an ultrahigh color rendering index of 93.9 were reported by Luo et al., in which the chiral structure endues this material with efficient nonlinear optical (NLO) response [63]. Obviously, reducing dimension at the molecular level is conducive to enhancing the chirality of HMHs and improving their photophysical properties, which renders them to be promising in various optoelectronic applications.

2.1.4. 0D structure

For 0D HMHs, individual inorganic metal halide units are completely isolated by separated organic cations. Our group introduced *R-/S*-MBA into the framework of the copper halide structure and fabricated 0D (*R-/S*-MBA)$_2$CuCl$_4$ with a record *g*$_{abs}$ as high as ~0.06, in which each [CuCl$_4$]$^{2-}$ tetrahedra is isolated separately and a 0D structure is formed [64]. Moreover, Tang et al. reported CPL in chiral 0D (*R-/S*-MBA)$_4$Cu$_4$Cl$_4$ clusters crystallized in the orthorhombic space group of *P*2$_1$2$_1$2$_1$ [65]. Simultaneously, other chiral organic

molecules can also be utilized to obtain chiral HMHs with diverse dimensional crystal structures. Recently, by means of regulating the stoichiometric proportion of the precursor, Li et al. reported two kinds of low-dimensional HMHs with the same conformational formula $(R\text{-MPA})_2CdCl_4$ (R-MPA = R-1-methyl-3-phenylpropylammonium) but different crystal structures [66]. As described in Fig. 4e, compared with achiral 1D structure, the asymmetric unit of the 0D chiral ferroelectric with polar Sohncke space group $P1$ consists of four organic MPA$^+$ cations and two discrete $[CdCl_4]^{2-}$ tetrahedra, resulting in distinct CD and increased ferroelectricity and SHG response [66]. Notably, due to the absence of rational and universal methods, there is still a lack of design and synthesis of 0D HMHs, which seriously hinders the exploration of related applications. As a result, relevant research work is urgently required to enrich the material family of low-dimensional chiral HMHs.

2.2. Helical structure and heterostructure

2.2.1. Helical structure

Helical structures of HMHs have also been proven to exhibit efficient optical activity. For example, crystalline disulfides R-S-S-R' (R and R′ represent achiral organic groups) can form helical structures and exhibit chiral P- and M-helical conformations [67]. Based on protonated cystamine $(H_3N(CH_2)_2S–S(CH_2)_2NH_3)^{2+}$ cations, a series of HMHs with helical structures were demonstrated. Mercier et al. reported the preparation and structural transformation of several chiral disulfide-based HMHs, *i.e.*, α-$(H_3N(CH_2)_2S–S(CH_2)_2NH_3)$ $PbI_5 \cdot H_2O$ and α-$(H_3N(CH_2)_2S–S(CH_2)_2NH_3)BiI_5$ that crystallized in the Sohncke space groups [68,69]. The crystal structure of the latter is composed of zigzag chains of corner-sharing bismuth iodide octahedra extending along the a-axis, which are separated by $(H_3N(CH_2)_2S–S(CH_2)_2NH_3)^{2+}$ cations in the P- or M-helical conformation along the b-axis. As shown in Fig. 5a, both P- or M-helical conformations exist in the crystal structure of the chiral disulfide-based hybrid bismuth halides, and the chiral molecules in the adjacent ab planes show opposite chirality. Due to the conformational change of the disulfide molecules in α-$(H_3N(CH_2)_2S–S(CH_2)_2NH_3)BiI_5$, the helical HMHs will undergo a reversible phase transition from acentric α-phase to centric β-phase when heated to 36.8 °C, making them potential candidates for switchable NLO materials [69].
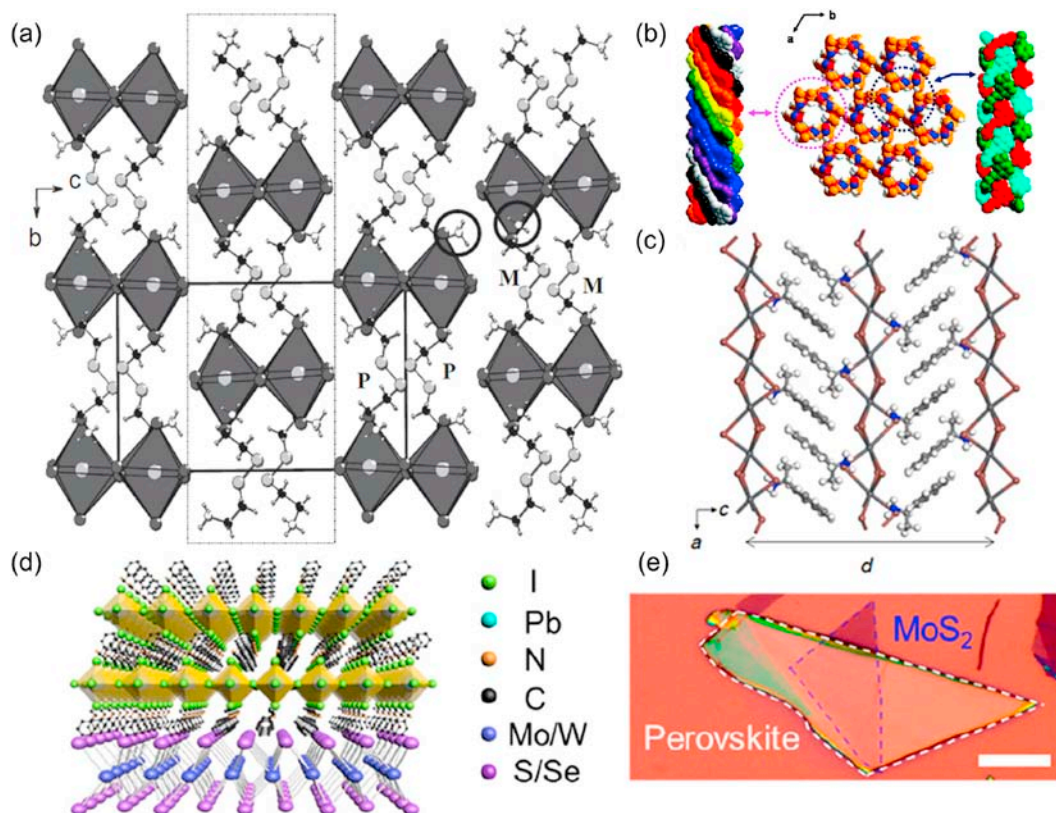

Fig. 5. Schematic diagram of chiral HMHs with helical structures and heterostructures. (a) Packing diagram of α-$(H_3N(CH_2)_2S–S(CH_2)_2NH_3)BiI_5$ viewed along the a-axis. Reproduced with permission from Ref. [69]: Copyright 2008, John Wiley and Sons. (b) Space-filling representation of Kagome-shaped tubular structure composed of achiral organic cations and 1D $[PbI_3]_\infty$ chains. Reproduced with permission from Ref. [70]: Copyright 2010, American Chemical Society. (c) Structural model of 1D helical (R-1-NEA)PbI$_3$ in the ac plane. Reproduced with permission from Ref. [71]: Copyright 2020, American Association for the Advancement of Science. (d) Schematic of crystal structure of a chiral 2D (R-/S-MBA)$_2$PbI$_4$/monolayer TMD heterostructure. (e) Optical image of the chiral 2D (R-/S-MBA)$_2$PbI$_4$/MoS$_2$ heterostructure. Reproduced with permission from Ref. [76]: Copyright 2020, American Chemical Society.

Furthermore, Zhao et al. obtained a series of ferroelectrics crystallized in space group $P6_3$ by introducing Schiff base 3-R-Benzyli-dene-1-aminopyridinium (m-RBz-1-APy$^+$, R = NO$_2$, Br, Cl, or F) cations [70]. As depicted in Fig. 5b, the crystal structure of the reported HMHs is composed of achiral organic cations and 1D [PbI$_3$]$_\infty$ chains connected by Coulomb and van der Waals force to form a Kagome-shaped tubular structure, in which organic cations are arranged in a helix around the tube axis. Besides, the introduction of chiral enantiomer molecule, *i.e.*, R-/S-1-(1-naphthyl)ethylamine (R-/S-1-NEA), can affect the distortion of the [PbI$_6$]$^{4-}$ octahedral structure and enhance their chirality, due to the strong interaction between the large π-conjugated naphthalene skeleton of 1-NEA$^+$ and adjacent molecules [71]. Recently, Ishii and Miyasaka presented the thin film fabrication of 1D helical and 2D HMHs composed of chiral enantiomer molecule (R-/S-1-NEA) [71]. Compared with the interaction between the [PbI$_6$]$^{4-}$ octahedral plane and chiral molecules in 2D structure, chiral 1-NEA$^+$ cations in 1D structure can cause a larger helicity of the chain, as a result of strong interaction between the [PbI$_6$]$^{4-}$ chain and chiral 1-NEA$^+$ cations (Fig. 5c). In addition, the resultant 1D helix possesses a highly g_{abs} of 0.04 [71].

2.2.2. Heterostructure

Transition metal dichalcogenides (TMDs) have aroused extensively research interest in recent years, owing to their unique electronic and photonic properties [72–74]. The combination of chiral HMHs and TMDs offers a wide variety of options for designing new types of heterojunctions with idiographic functionalities and applications. For example, due to the robust interlayer coupling, the chiral (S-MBA)$_2$PbI$_4$/monolayer WSe$_2$ heterojunction demonstrated a high degree of circularly polarized interlayer exciton emission of 13% [75]. Based on selective spin injection, Li et al. developed a simple and efficient way to manipulate the valley pseudo-spin by constructing chiral HMHs/monolayer TMD heterostructures without circularly polarized light excitation or an additional magnetic field [76]. The chiral 2D (R-/S-MBA)$_2$PbI$_4$ and monolayer TMDs, which were mechanically exfoliated from the corresponding bulk crystals, can form heterojunctions through the dry-transfer method [76]. Fig. 5d and e shows the schematic crystal structure and optical image of the chiral 2D (R-/S-MBA)$_2$PbI$_4$/monolayer TMD heterostructure, respectively. Chiral 2D (R-/S-MBA)$_2$PbI$_4$ with opposite chirality tends to inject specific spin-polarized carriers into the target valley of monolayer TMDs due to the chiral-induced spin selectivity (CISS) effect, thereby realizing the manipulation of valley pseudospin in monolayer TMDs [76]. Recently, using the two-step solution-epitaxial method, Luo et al. fabricated (R-/S-MPEA)$_2$MAPb$_2$I$_7$/MAPbI$_3$ (R-/S-MPEA = R-/S-β-methylphenethylammonium; MA = methyl-ammonium) heterostructure crystals and obtained a circularly polarized light detector with greatly amplified sensitivity [77]. Overall, in-depth study on the photophysical process of such heterojunction materials provides a promising platform for broadening the application prospects of chiral HMHs.
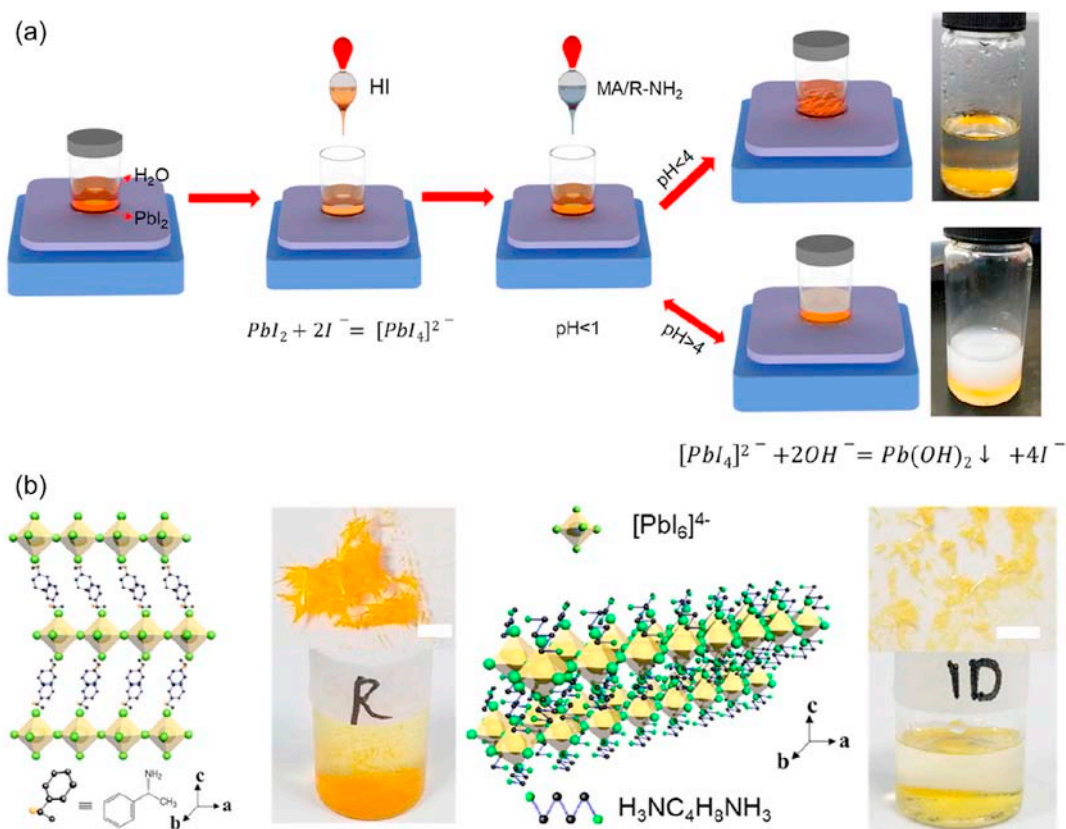

Fig. 6. (a) Schematic illustration of the aqueous synthetic strategy at room temperature. (b) Crystal structures and optical microscope images of the 2D (R-MBA)$_2$PbI$_4$ (left) and 1D C$_4$N$_2$H$_{14}$PbI$_4$ (right) single crystals synthesized by the aqueous method. Reproduced with permission from Ref. [131]: Copyright 2019, American Chemical Society.

3. Synthetic methods and stability

3.1. Crystal growth methods

At present, a variety of synthetic strategies have been exploited to synthesize single crystals of chiral HMHs with the development of synthetic technique, including temperature-lowering crystallization [19,20,44,46,47,57,61–63,68,75–106], solvent evaporation crystallization [45,54,66,69,70,107–129], antisolvent vapor-assisted crystallization [130], aqueous synthetic strategy [131]. Briefly, temperature-lowering crystallization and solvent evaporation crystallization methods are implemented based on the following principle. The solubility of metal halide precursors in the hydrohalic acid aqueous solution decreases with the decrease of the solution temperature [132,133], or the evaporation of the solvent increases the concentration to the saturation point of the precursor solution to induce crystallization [134,135]. In this section, we focus on the antisolvent vapor-assisted crystallization method and aqueous synthetic strategy.

The antisolvent vapor-assisted crystallization is based on the different solubility of metal halide precursors in different solvents [28]. Typically, metal halide precursors exhibit high solubility in strong polar solvents, such as *N,N*-dimethylformamide (DMF), dimethyl sulfoxide (DMSO), *γ*-butyrolactone, while they exhibit low solubility in weak or even nonpolar solvents, including toluene, chlorobenzene, ether, chloroform and methanol. These solvents with low solubility for metal halide precursors are known as antisolvents while those with high solubility are called good solvents. Yuan et al. utilized a mixture of DMF and DMSO as the good solvent instead of pure DMF to improve the crystal size and the optical quality of chiral single crystals [130]. The DMSO molecules directly participated in the formation of the *α*-phase crystal structure, and the chemical formula of the chiral single crystals was determined as (*R-/S*-MPEA)$_{1.5}$PbBr$_{3.5}$(DMSO)$_{0.5}$. Concretely, the slow diffusion of chloroform vapor into the precursor solution (consisting of PbBr$_2$ and MPEA$^+$Br$^-$ precursors dissolved in a mixed solvent of DMF and DMSO) led to solution supersaturation and triggered the formation and growth of chiral crystals [130]. Such a facile antisolvent method possesses a high degree of compatibility and can potentially be applied to the growth of other single crystals of chiral HMHs.

The aqueous synthetic strategy was recently reported by Li et al. [131]. Without using chemically toxic solvents, the reported aqueous method can produce almost twice the yield compared with previously reported method (~80% based on the total Pb content) and is universally applicable to the synthesis of the single crystals of low-dimensional HMHs at room temperature [131,136]. As
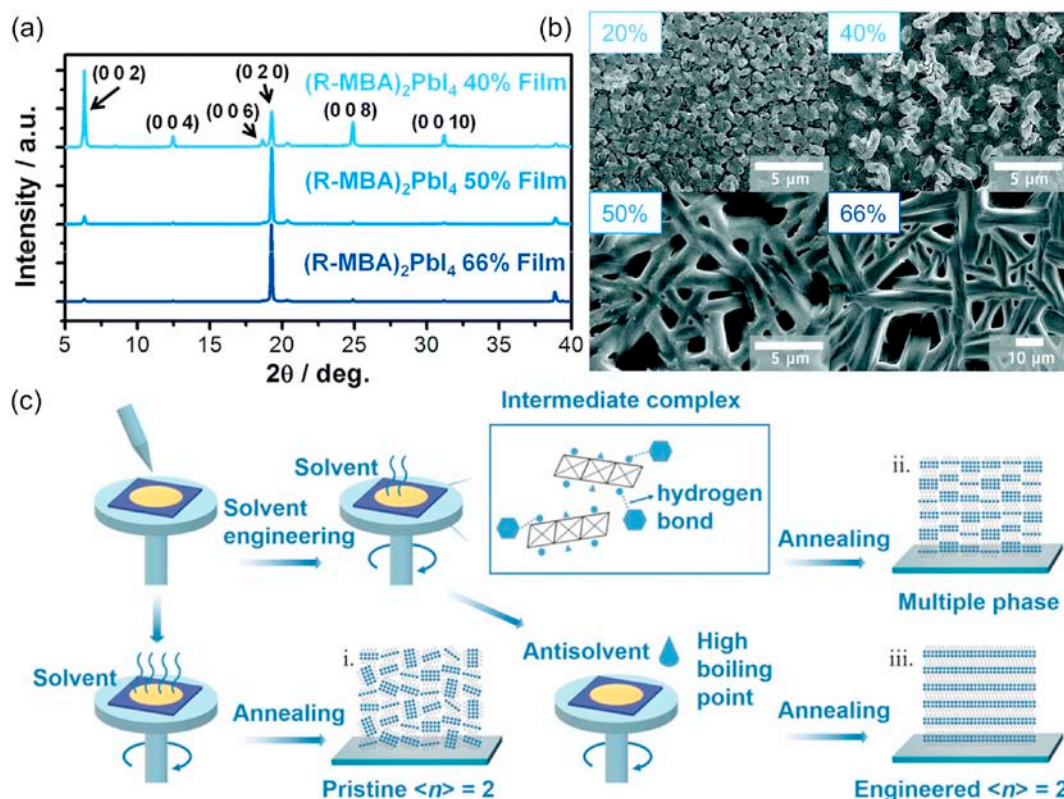

Fig. 7. (a) X-ray diffraction patterns of the (*R*-MBA)$_2$PbI$_4$ thin films prepared using precursor solutions with concentrations of 40, 50 and 66 ωt%. (b) Scanning electron microscope images of the (*R*-MBA)$_2$PbI$_4$ thin films prepared using different concentrations of precursor solutions. Reproduced with permission from Ref. [47]: Copyright 2017, Royal Society of Chemistry. (c) Crystallization dynamics regulating mechanism of the thin films of chiral quasi-2D HMHs. Reproduced with permission from Ref. [61]: Copyright 2020, John Wiley and Sons.

illustrated in Fig. 6a, the aqueous hydriodic acid solution was dropped into the mixture of PbI$_2$ and deionized water under constant stirring, and then an aqueous solution of CH$_3$NH$_2$ (MA) and large organic amino cation (R–NH$_3$) was injected into the above solution. Note that the pH value of the solution is critical for the formation of the final product. High-quality single crystals can be formed when the pH value is lower than 4, while milky white precipitates will be formed when the pH value exceeds 4 [131]. In addition, Fig. 6b presents the crystal structures and optical microscope images of the 2D and 1D single crystals synthesized by this aqueous method. It is worth noting that the chiral 2D (R-/S-MBA)$_2$PbI$_4$ synthesized by this method exhibits CPL at room temperature with a high polarization degree of 13.7% or 11.4%, respectively [131]. The excellent crystalline quality together with the enhanced stability of the as-grown single crystals of 2D and 1D HMHs would make this synthetic method attractive for preparing low-dimensional HMHs for fundamental investigations and various optoelectronic applications.

3.2. Spin-coating approach

The most representative method to prepare thin films of chiral HMHs is one-step solution-processed approach, in which optimized stoichiometric ratio of metal halides and chiral organic ammonium halide salts or designed mass fraction of pre-grown single crystals are dissolved in certain polar solvents. The resultant precursors are then dropped on substrates followed by a spin-coating approach. Because the chiral enantiomer (R-/S-MBA) is commercially available with low cost and their ammonium salts exhibit good solubility in strong polar organic solvents [137], they can be facilely applied to fabricate thin films of chiral HMHs and has been demonstrated in a wide variety of photonic and electronic applications [20,62,64,76,81,87,93,96]. Moon et al. pioneered to investigate the effect of spin-coating conditions on the morphology and chiroptical properties of (R-/S-MBA)$_2$PbI$_4$ thin films [47]. As described in Fig. 7a and b, the crystallographic orientation of the chiral thin films prepared using the 20 ωt% precursor solution was along the (0 0 2) plane, causing the formation of planar crystals. On the contrary, with the increase of solution concentration, the chiral thin films would tend to be gradually oriented along the (0 2 0) plane and display a needle-like morphology. They also found that the film orientation was not only affected by the concentration of the precursor solution, but can also be varied by the annealing temperature or the solvent used to form the precursor solution [47].

The precursor solution can be formed by dissolving the pre-grown single crystals or as-synthesized chiral ammonium salts and the metal halides with a certain stoichiometric ratio into a polar solvent. In latter case, the adjustment of relevant stoichiometric ratio can realize the control of final products. For example, the thin film dimensionality of chiral HMHs can be modified by adjusting the stoichiometric molar ratio of the precursors during the synthesis stage [71]. In the above case, the addition of MA can slow down the crystal formation speed of the 1D structures and is conducive to obtaining a smooth surface, causing the CD signals of the as-synthesized 1D helical HMHs 10 times larger than that without MA [71]. Moreover, this phenomenon was also observed in other crystals, in which the addition of MA would help to maintain the appropriate ion balance but not lead to the formation of MAPbI$_3$ phase [131,138]. Therefore, the addition of MA may have a positive influence on the optical activities, which also provides a significant guidance to control the thin film fabrication of chiral HMHs.

Effective control of the film formation kinetics of chiral HMHs is of great importance for practical applications. It has been proved that reducing the crystallization rate and maintaining a homogeneous distribution of organic cations are the keys to obtain parallel-oriented quasi-2D thin films with homogeneous energy landscape [139,140]. On this basis, Wang et al. modulated the film crystallization kinetics through solvent engineering to facilitate carrier transport [61]. During the synthetic process, pure DMSO was employed as the solvent instead of DMF. It provided alternative sites for chiral organic cations by forming the solvent–MA$^+$/PbI$_x^-$ intermediate compounds and slowed down the crystallization rate, thereby initiating preferential in-plane crystallization. In addition, the chlorobenzene with high boiling point was employed as an antisolvent to regulate the crystallization kinetics, resulting in the formation of a parallel-oriented thin film of chiral quasi-2D HMHs with homogeneous energy landscape, as shown in Fig. 7c. More importantly, the as-formed thin film can be used as a high-performance circularly polarized light detector with enhanced carrier transport and collection efficiency [61]. It is worth noting that most of abovementioned thin films were prepared by the spin-coating approach. Therefore, this approach can provide a simple but very effective method to fabricate chiral thin films toward various optoelectronic devices.

3.3. Stability

In order to realize real commercialization of chiral HMHs, they should have good stability in the atmosphere environment. Although traditional ternary metal halides tend to be chemically unstable and easily react with oxygen and water molecules to cause phase separation [22], the chiral HMHs usually possess improved stability. For example, the X-ray diffraction patterns of (R-/S-MBA)$_2$PbI$_4$ thin films exhibited no obvious difference within 7 days under controlled temperature (25.0 ± 0.5 °C) and relative humidity (20.0 ± 1.0%) [47]. Also, the CD spectra of (R-/S-MBA)$_2$CuCl$_4$ hardly changed after storage under ambient condition over one month [64]. Compared with 2D (R-/S-MBA)$_2$PbI$_4$, the 1D (R-/S-MBA)PbI$_3$ thin films exhibited significantly enhanced stability and almost the same spin transport properties within one month [99]. Even so, the development of chiral HMHs with high stability against oxygen, moisture and temperature is still urgently needed to avoid obstacles to practical applications.

4. Fundamental physics and strategies for the modulation of optical activity

4.1. Fundamental physics

Among various spectroscopic tools for the characterization of chiral materials, CD and CPL are the most widely used methods, which

can probe chirality in the ground and excited states, respectively. Typically, circularly polarized light can be obtained from unpolarized light, with the help of a linear polarizer and a $\lambda/4$ waveplate (Fig. 8a). The measurement principles of CD and CPL spectra are illustrated in Fig. 8b and c. Succinctly, CD can be ascribed to the differential absorption of left- and right-handed circularly polarized (LCP and RCP) light [141]. Similarly, CPL is due to the difference in LCP and RCP emission [142].

As a function of wavelength, the CD intensity is determined by the difference in absorbance between the LCP and RCP components ($\Delta A = A_L - A_R$, where A_L and A_R refer to the absorbance for LCP and RCP light, respectively) [143]. According to the Beer-Lambert law, the ordinate of the CD spectra represents the ellipticity θ in unit of mdegree, which has a specific numerical relationship with ΔA, i.e., $\theta = 32982 \times \Delta A$ [144]. Experimentally, the magnitude of CD can be quantified by the absorption dissymmetry factor (g_{abs}, also known as g_{CD}) through following equation [144]:

$$g_{abs} = \frac{\Delta A}{A} = \frac{\theta}{32982 \times A} \tag{1}$$

where A is the absorbance of the chiral sample.

The CPL intensity can be quantified by the emission dissymmetry factor (g_{lum}, also known as g_{em}) that can estimate the asymmetry degree of LCP and RCP emission. It can be calculated according to following equation [145]:

$$g_{lum} = \frac{2(I_L - I_R)}{I_L + I_R} \tag{2}$$

where I_L and I_R refer to the intensity of LCP and RCP emission, respectively.
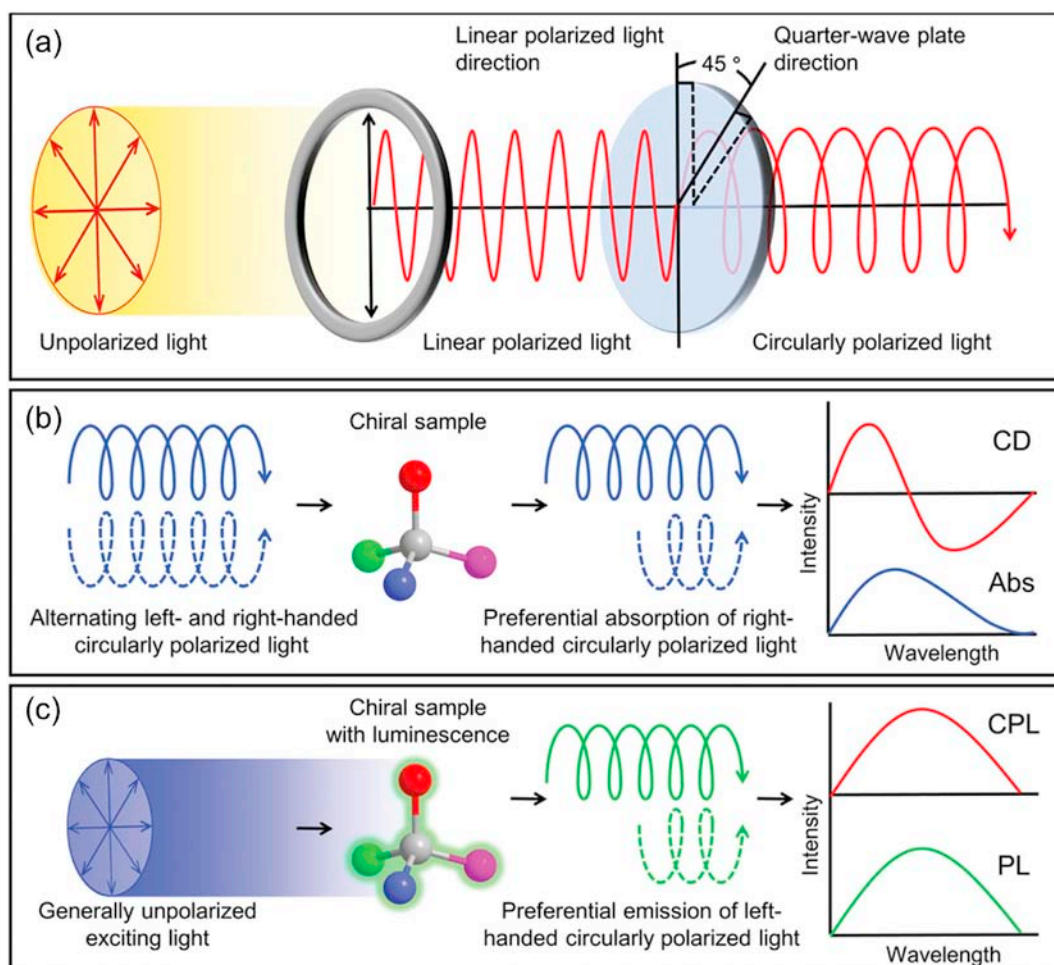

Fig. 8. Fundamental properties of chiral HMHs. (a) Relationship between unpolarized light, linearly polarized light and circularly polarized light. Schematic illustration of (b) CD and (c) CPL. Reproduced with permission from Ref. [14]: Copyright 2020, John Wiley and Sons.

4.1.1. The origin of CD

From the perspective of quantum theory, the CD intensity in a chiral molecule is proportional to the rotational strength (R), which results from the electric transition dipole moment interfering with the magnetic transition dipole moment and can be expressed as [146, 147]:

$$CD_{molecule} \propto R = Im\left[\Psi_s|\widehat{\mu}|\Psi_j \cdot \Psi_j|\widehat{m}|\Psi_s\right] = Im\left[\mu_{sj} \cdot m_{js}\right] \tag{3}$$

where Ψ_s and Ψ_j are the wave functions of the ground state (s) and excited state (j), Im is the imaginary part of the parameter, $\widehat{\mu}$ and $\widehat{m}$ are the corresponding electric and magnetic moment operators, and μ_{sj} and m_{js} are the electric and magnetic transition dipole moments, respectively. Since Equation (3) can be applied to all quantum systems [18], it can serve as a reference for identifying the origin of CD in chiral HMHs. The condition for the observation of CD signal is that the electric and magnetic dipole moment operators must be converted into the same irreducible representation [60]. Under the constraints of the stringent selection rule, the possible molecular point groups with CD signals are only C_n, D_n, O, T, and I [60,148]. In other words, the chirality of HMHs is a consequence of their inherent crystallographic point group, which enables μ_{sj} and m_{js} non-zero and induces optical activity (*i.e.*, CD). It is noteworthy that the coupling effect of dipole transition moments between inorganic framework and organic molecule is also considered to be a possible mechanism that may cause the chirality of chiral HMHs [19,81,106]. However, the actual mechanism still requires further investigation.
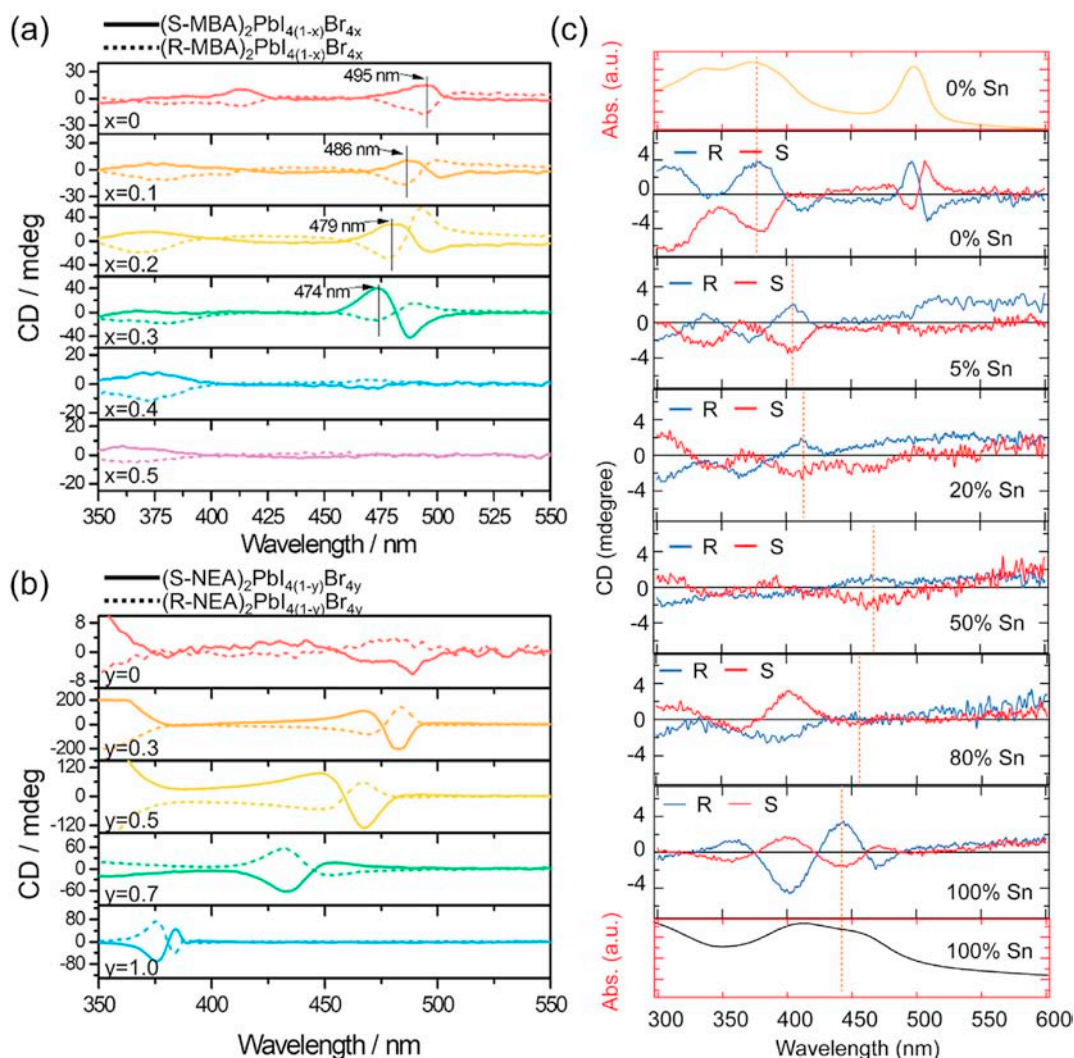

Fig. 9. Wide wavelength range tunable CD of chiral HMHs. (a) CD spectra of (R-/S-MBA)$_2$PbI$_{4(1-x)}$Br$_{4x}$ ($x = 0$, 0.1, 0.2, 0.3, 0.4, and 0.5) thin films. (b) CD spectra of (R-/S-2-NEA)$_2$PbI$_{4(1-y)}$Br$_{4y}$ ($y = 0$, 0.3, 0.5, 0.7, and 1.0) thin films. Reproduced with permission from Ref. [43]: Copyright 2020, American Chemical Society. (c) CD spectra of (R-/S-MBA)$_2$Pb$_{1-x}$Sn$_x$I$_4$ ($x = 0$, 0.05, 0.20, 0.50, 0.80, 1) solid solution thin films. Reproduced with permission from Ref. [44]: Copyright 2020, American Chemical Society.

4.1.2. Design principle

Although great progress in the investigation on the chiroptical properties of HMHs has been made, there is still extensive room for exploring new chiral HMHs with large anisotropy factors. Towards this end, the design, synthesis, and characterization of HMHs with large anisotropy factors (g_{abs} and g_{lum}) are extensively required for the realization of relevant high-demand applications. However, the mechanism of enhanced optical activity of chiral HMHs is still being explored. Theoretically, the g_{abs} can be expressed as [149]:

$$g_{abs} = \frac{4|\mu| \cdot |m| cos\theta}{|\mu|^2 + |m|^2} \qquad (4)$$

wherein θ is the angle between the electric and magnetic transition dipole moments. Usually it satisfied the condition $|\mu| \gg |m|$ at the molecular scales, and g_{abs} is proportional to magnetic transition dipole moment but inversely proportional to electric transition dipole moment [18]. Previous literature indicated that the hybrid lead iodides containing chiral 2-NEA exhibited larger g_{abs} than that containing chiral MBA, which can be explained by the larger magnetic transition dipole moment of the former [43]. Additionally, because the ground state wave function Ψ_s is the same for any CD transition, the difference in the magnitude and algebraic sign of various transitions mainly comes from the change of the excited state wave function Ψ_j (Equation (3)) [148]. Based on time-dependent density functional theory, we calculated the optical selectivity of circularly polarized light versus the band gap of the chiral (R-/S-MBA)$_2$CuCl$_4$ thin films [64]. Especially, compared with the other MBA-containing chiral hybrid lead halides, the larger CD signals in the chiral (R-/S-MBA)$_2$CuCl$_4$ thin films were proved to be induced by their higher joint density of states. Furthermore, owing to the lower absorption of chiral organic molecular precursors, Hu et al. attributed the larger CD signals of chiral HMHs to larger electric field–dipole interaction, i.e., larger absorption coefficient that was estimated from Equation (3) [86]. Recently, Lin et al. changed the halogen atoms of organic ions to modulate the CD and CPL of chiral 2D HMHs and demonstrated that the magnetic transition dipole is sensitive to the d-spacing between inorganic layers and the halogen-halogen interaction between the organic cations and inorganic sheets [98]. These studies can provide some theoretical guidance to explore chiral HMHs with larger anisotropy factors. For example, the design of chiral HMHs with larger magnetic transition dipole moment or joint density of states or absorption coefficients may be effective ways to amplify their anisotropy factors. Regrettably, the relevant experimental investigation is still scarce, and more efforts are needed to verify the feasibility of these conjectures.

4.2. Strategies for the modulation of optical activity

4.2.1. CD of chiral HMHs

The investigation on the chemical-composition (chiral organic molecules, halogens, and metal elements) influences on the chiroptical properties of chiral HMHs is of great significance for the structural engineering of high-performance optoelectronic devices. For example, Moon et al. examined the CD tunability of chiral HMHs by modifying the chemical composition [43]. As shown in Fig. 9a, replacing iodide anions with bromides would result in an obvious blueshift of the CD signals of chiral (R-/S-MBA)$_2$PbI$_{4(1-x)}$Br$_{4x}$ thin films, which indicated that the widening of the band gap could induce a change in the excitonic band structure. Notably, when x = 0.4 or 0.5, the CD signals disappeared, as a result of the phase transition of the crystalline structure caused by the modulation of the halide anion mixing ratio [43]. In addition, increasing the spacer size of organic ammonium cations in 2D HMHs would cause a blueshift of the absorption peak [150]. To obtain a larger band gap, the chiral enantiomer R-/S-1-(2-naphtyl)ethylamine (R-/S-2-NEA) molecule with an enlarged spacer size was introduced into the inorganic framework [43]. For (R-/S-2-NEA)$_2$PbI$_{4(1-y)}$Br$_{4y}$ thin films, their CD peak position could be adjusted to near 375 nm (Fig. 9b). In addition, the bromide-determinant phase can induce enhanced CD signals compared with the iodide-determinant phase. Further, the band gap of chiral HMHs can be tuned by altering metal elements. For instance, Lu et al. reported the synthesis of two highly distorted tin-based chiral HMHs, which exhibited optical activity in the wavelength range of 300–500 nm [44]. Fig. 9c shows the modulability of the CD signals by tuning the composition of the metal elements in (R-MBA)$_2$Pb$_{1-x}$Sn$_x$I$_4$. Interestingly, because changes in chirality should have the same influence behavior on different peaks, the second lowest energy peak of interest (orange dashed-line) showed a redshift from 380 to 466 nm when the Sn concentration increased from 0 to 50%. However, further increasing the Sn concentration would lead to a blueshift of CD peak position (Fig. 9c). This bowing shift in CD peak was consistent with their nonlinear change of band gap. It originated from the energy mismatch between s and p orbitals of Pb and Sn, which generated the band gap between the Sn-derived valence band maximum and Pb-derived conduction band minimum in the alloys [151]. Under these circumstances, through the band gap engineering, the CD signals of HMHs can be tuned in a wide wavelength range, furnishing tremendous possibilities for various optoelectronic applications.

4.2.2. CPL of chiral HMHs

The development of CPL-active materials has triggered tremendous attention due to their widespread applications, such as 3D display [152,153], information encoding [154,155] and optical communication [156,157]. In particular, chiral HMHs, as a new type of CPL-active materials, have recently drawn extensive interest. The rational design and development of novel chiral HMHs with strong chirality are imminent, which is very meaningful for the realization of relevant practical applications.

1) CPL in Chiral Structures

The incorporation of chiral organic molecules and inorganic metal halides endows HMHs with CPL characteristics without applying an external magnetic field [15,54,60,82,117,125,131]. In general, the degree of polarization (DP) of CPL is defined as:

$$DP = \frac{I_{\sigma^+} - I_{\sigma^-}}{I_{\sigma^+} + I_{\sigma^-}} \tag{5}$$

where I_{σ^+} and I_{σ^-} represent the intensity of the LCP (σ^+) and RCP (σ^-) emission, respectively. As a result of the larger mole fraction of chiral molecules (67%) in chiral pure 2D HMHs, it is expected that chiral pure 2D HMHs should have a larger DP compared with chiral quasi-2D HMHs [82]. As depicted in Fig. 10a–c, from the as-exfoliated (R-/S-MBA)$_2$PbI$_4$ microplates, Li et al. obtained CPL with an average DP value of 9.6% and 10.1% at 77 K, respectively [82]. However, the (rac-MBA)$_2$PbI$_4$ (rac-MBA denotes racemic α-methyl-benzylammonium) exhibited no difference between LCP and RCP emission. Temperature-dependent measurement indicated that the DP decreased monotonously with the increasing temperature and nearly vanished at room temperature (Fig. 10d). The negative correlation between DP and temperature may origin from the reduction of lattice distortion induced by the chiral molecules or the increase of the spin flip at higher temperature [82]. Nuzzo et al. observed CPL peaking at 540 nm at room temperature from the chiral quasi-2D thin films (top in Fig. 10e) [15], which were obtained by mixing (R-/S-1-NEA)Br with CsBr and PbBr$_2$. The blue-shift of the unpolarized PL spectra from the phase with $\langle n \rangle > 4$ was proposed to be derived from a subset of states in the semiconductor (bottom in Fig. 10e) [15]. Based on Equation (4), the lower limit of magnetic transition dipole moment was determined as $0.1\mu_B$, where μ_B is the Bohr magneton. Moreover, Li et al. also achieved room-temperature CPL with high DP by developing an aqueous synthetic strategy [131]. Since DP decreases significantly with increasing temperature, its value at room temperature is usually extremely low.

2) CPL in achiral structures

As mentioned earlier in this review, optical activity can also be expected from four types of achiral crystal structures, including point groups C_s, C_{2v}, S_4 and D_{2d} (Fig. 3) [115,158]. Their optical activities depend solely on their symmetry and are independent of the intrinsic atomic arrangement therein [159,160]. For the first time, Zhao et al. reported the CPL activities of achiral (K(dibenzo-18-c-rown-6))$_2$MnX$_4$ (abbreviated as (KC)$_2$MnX$_4$, X = Cl and Br) single crystals with an achiral C_s point group [115]. The crystal structure of (KC)$_2$MnCl$_4$ is described in Fig. 11a and b, where each central Mn atom coordinates with four Cl atoms to form [MnCl$_4$]$^{2-}$ tetrahedra that is co-crystallized with two KC cations though electrostatic interactions. Then, the (KC)$_2$MnCl$_4$ units are arranged in a left-handed or right-handed helix through K$^+$–π interactions, where the opposite helixes can be converted to each other through the slide and mirror symmetry operations [115]. CPL was further observed in the achiral (KC)$_2$MnBr$_4$ and (KC)$_2$MnCl$_4$ single crystals. With the help of a λ/4 waveplate and a linear polarizer, CPL was converted into linearly polarized light in the direction of +45° and −45° to the fast axis of the λ/4 waveplate. As depicted in Fig. 11c and d, the final polarization direction of the linearly polarized light was determined to be perpendicular, which further proved the CPL in the achiral (KC)$_2$MnBr$_4$ single crystals [115]. Since the report on the optical activity in achiral crystals is scarce, the above-mentioned findings provide new insights into the design of achiral single crystal HMHs with efficient optical activity.
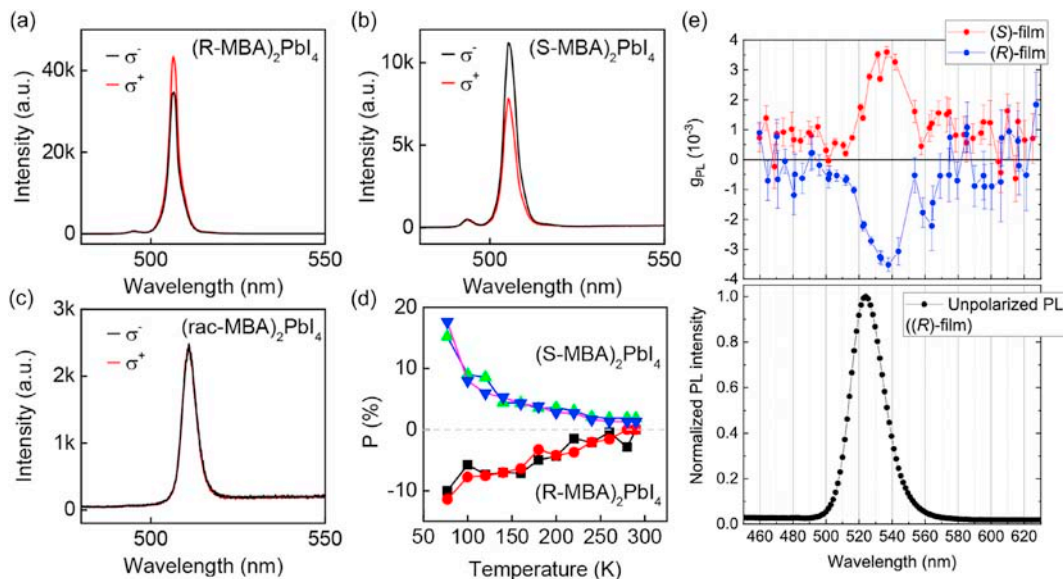

Fig. 10. CPL in chiral structures. LCP (σ^+) and RCP (σ^-) emission spectra of the chiral (a) (R-MBA)$_2$PbI$_4$, (b) (S-MBA)$_2$PbI$_4$, and (c) (rac-MBA)$_2$PbI$_4$ microplates. All the samples were excited by a 473 nm laser at 77 K. (d) DP as a function of temperature for the chiral (R-/S-MBA)$_2$PbI$_4$ microplates. Reproduced with permission from Ref. [82]: Copyright 2019, American Chemical Society. (e) CPL (top) and unpolarized PL (bottom) spectra of the chiral quasi-2D thin films excited by unpolarized light at room temperature. Reproduced with permission from Ref. [15]: Copyright 2020, American Chemical Society.
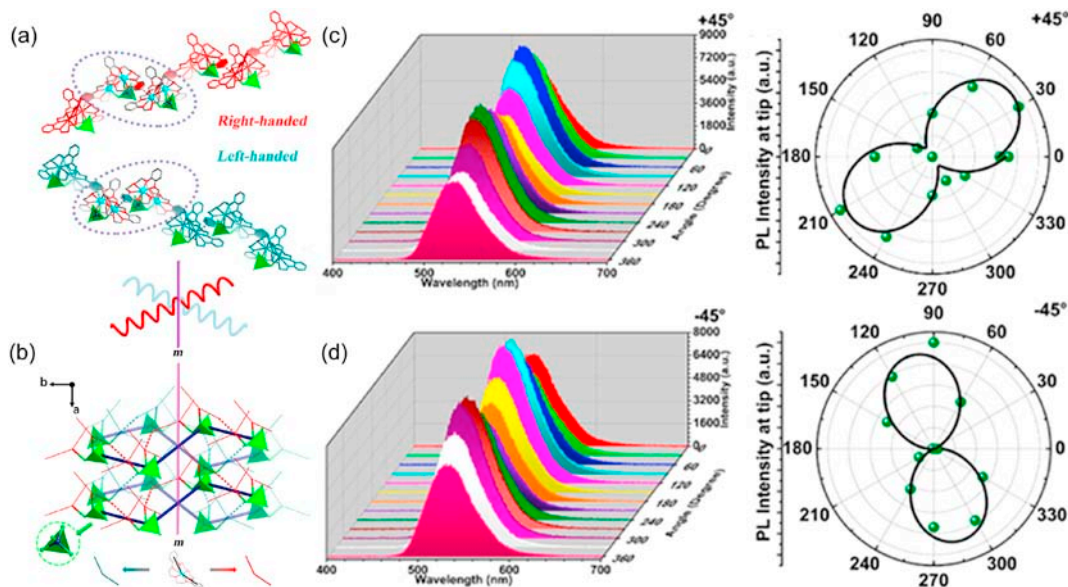
Fig. 11. CPL in achiral structures. (a) Right- and left-handed helix in $(KC)_2MnCl_4$ complexes and schematic diagram through the plane of symmetry in the *m* point group. (b) Simplified stacking of helixes of $(KC)_2MnCl_4$ viewed along the *c*-axis with a mirror. Polarized PL spectra and PL intensity of the $(KC)_2MnBr_4$ microrod as a function of the polarizer rotation angle. Angle of the $\lambda/4$ waveplate is (c) $+45°$ and (d) $-45°$, respectively. Reproduced with permission from Ref. [115]: Copyright 2019, American Chemical Society.

5. Optoelectronic applications

5.1. Circularly polarized light photodetectors

The conventional detection of circularly polarized light is generally accomplished with the help of a $\lambda/4$ waveplate and a linear polarizer. In virtue of the different polarized electronic spin directions generated by selective absorption of circularly polarized light [71,
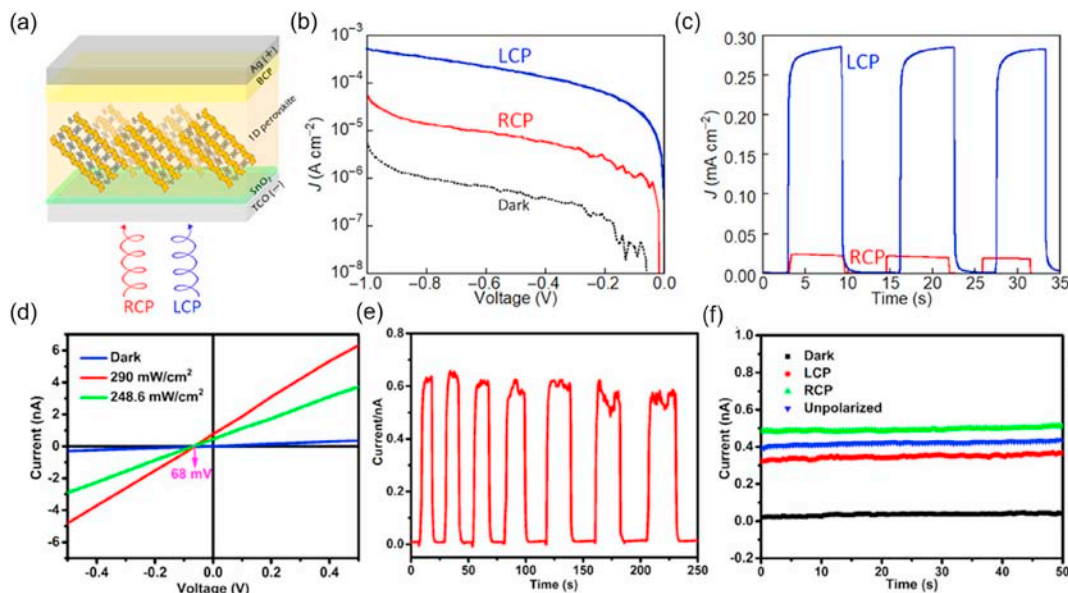

Fig. 12. Application of chiral HMHs as circularly polarized light photodetectors. (a) Schematic diagram of the photodetector based on 1D helical (*R-/ S*-1-NEA)PbI_3. (b) *J–V* curves of the (*R*-1-NEA)PbI_3 device under the excitation of LCP and RCP light at 395 nm. (c) Time course of photoresponse (*J–T* curves) for the (*R*-1-NEA)PbI_3 device at an applied voltage of -0.5 V. Reproduced with permission from Ref. [71]: Copyright 2020, American Association for the Advancement of Science. (d) Bulk photovoltaic effect in the (*R*-MPEA)$_4AgBiI_8$ crystal excited by a 520 nm laser. (e) Time-dependent reproducible photocurrent on/off switching at zero bias. (f) Self-powered current–time curves for the (*R*-MPEA)$_4AgBiI_8$ crystal device under 520 nm illumination. Reproduced with permission from Ref. [88]: Copyright 2021, John Wiley and Sons.

161], chiral materials with strong spin–orbit coupling (SOC) provide us with a possibility to directly detect circularly polarized light [162,163]. Because of the combination of sensitive chiroptical responsiveness and effective charge transport imparted by chiral organic components and inorganic components, a series of chiral HMHs have been used to directly detect circularly polarized light [61,62,71,77, 82,88,93,100,102,131,164–166]. For instance, Tang et al. developed chiral 1D (R-/S-MBA)PbI$_3$ for circularly polarized light photodetectors, with a responsivity of 797 mA W^{-1}, a detectivity of 7.1×10^{11} Jones and 3 dB frequency of 150 Hz [62]. The responsivity was nearly two orders of magnitude larger than that of chiral helicene and metamaterials [162,163]. Wang et al. manufactured circularly polarized light photodetectors using single crystal and thin film of chiral quasi-2D (R-MPEA)$_2$MAPb$_2$I$_7$ [61]. It was found that the single crystal photodetector exhibited a responsivity of 3.8 A W^{-1} and a detectivity of 1.1×10^{12} Jones.

Very recently, Ishii and Miyasaka fabricated a direct circularly polarized light photodetector with a bilayer structure (Fig. 12a), consisting of transparent conducting oxide (TCO), SnO$_2$ (10 nm, electron-transport/hole-blocking layer), (R- and S-1-NEA)PbI$_3$ (220 nm, circularly polarized light absorber), bathocuproine (BCP) (15 nm, hole-transport/electron-blocking layer) and Ag (80 nm) [71]. Fig. 12b shows the photocurrent density–voltage (J–V) characteristics of the (R-1-NEA)PbI$_3$ photodetector under the excitation of LCP and RCP light at 395 nm with an intensity of 1 mW cm^{-2}. Under an applied voltage of -0.5 V, the photocurrent signals were 2.8×10^{-4} and 1.2×10^{-5} A cm^{-2}, respectively (Fig. 12c). Additionally, the responsivity anisotropy factor (g_{res}) describes the distinguishability to circularly polarized light, which is defined as [62]:

$$g_{res} = \frac{2(R_L - R_R)}{R_L + R_R} \tag{6}$$

where R_L and R_R are the responsivities under LCP and RCP light illumination, respectively. Surprisingly, the polarization discrimination ratio R_L/R_R of (R-1-NEA)PbI$_3$ photodetector is as high as 25.4, far exceeding the previously reported values, such as 1.1 for chiral 1D (R-/S-MBA)PbI$_3$ [62], 1.22 for chiral quasi-2D (R-MPEA)$_2$MAPb$_2$I$_7$ [61], and 3.4 for chiral metamaterials [163]. The higher photoconductivity of chiral (R-1-NEA)PbI$_3$ can be attributed to its 1D helical structure and is related to the polarized electronic spin directions induced by selectively absorbing circularly polarized light with orbital angular momentum [71,161].

In conventional photovoltaic devices, photoexcited carriers are separated by a built-in electric field generated in the *p-n* junctions [167]. In contrast, bulk photovoltaic effect refers to the generation of a steady photocurrent in a single-phase homogeneous material lacking inversion symmetry [168]. It provides another way to separate photoexcited carriers and generate photovoltaic effect without a bias voltage [80,169]. The spatial inversion symmetry breaking endows chiral HMHs with potential self-powered circularly polarized light detection without an extra electric field. For instance, Li et al. investigated the intrinsic circularly polarized light detection capability of chiral lead-free (R-MPEA)$_4$AgBiI$_8$ crystals and the influence of bulk photovoltaic effect on circularly polarized light detection along the polar *b*-axis [88]. As a result of strong lattice distortion and electronic transitions between different metals in the layered structure [170], the responsivity and detectivity of the photodetector based on (R-MPEA)$_4$AgBiI$_8$ crystal were as low as 22 μA W^{-1} and 1.2×10^7 Jones, respectively [88]. Furthermore, on account of a built-in electric field generated by the bulk photovoltaic effect, a photovoltaic voltage of 68 mV was obtained under unpolarized 520 nm illumination, and the photovoltaic current exhibited good reproducibility under on/off switching, as described in Fig. 12d and e. Moreover, as presented in Fig. 12f, distinctly different photocurrent signals illuminated by LCP and RCP light was observed at zero bias and a photocurrent anisotropy factor of 0.3 was achieved for the self-powered circularly polarized light photodetector. Overall, chiral HMHs combine the sensitive chiroptical responsiveness of organic components and efficient charge transfer of inorganic components, affording an unprecedented and advantageous platform for direct detection of circularly polarized light.

5.2. Ferroelectrics

Regarded as an important topic in materials physics, ferroelectrics have been widely used in various applications, including sensors, energy storage and capacitors [171]. Ferroelectric materials are a subcategory of pyroelectric materials that belong to a subcategory of piezoelectric materials [172,173]. From the crystallographic point of view, ferroelectrics are inseparable from symmetry breaking. In other words, ferroelectric materials are non-centrosymmetric and must be crystallized among the ten types of polar point groups, *i.e.*, C_1, C_s, C_2, C_{2v}, C_3, C_{3v}, C_4, C_{4v}, C_6 and C_{6v} (Fig. 3) [174]. In recent years, as a class of emerging materials, chiral HMHs are considered as promising potential molecular ferroelectrics with desirable semiconductor characteristics, due to their easy-to-design material structure and inherent structural asymmetry [57,66,70,86,97,111,114,117,121,122,175]. However, the relationship between chirality and ferroelectricity has been ignored for a long time. For instance, by introducing chiral R-/S-CPEA cations into lead iodide octahedral inorganic framework, Xiong et al. successfully obtained the chiral 2D (R-/S-CPEA)$_2$PbI$_4$ ferroelectrics [57], which were crystallized in polar space group *P*1 at room temperature and exhibited a high phase-transition temperature of 483 and 473.2 K, respectively.

Apparently, the introduction of chiral enantiomer molecules is a unique and effective strategy for designing ferroelectric materials that are crystallized among the chiral Sohncke space groups (partially containing ten types of polar point groups, Fig. 3). Following the concept of introducing chirality, Hu et al. successfully designed and synthesized chiral 1D (R-/S-CHEA)PbI$_3$ (R-/S-CHEA = R-/S-1-cyclohexylethylammonium) switchable photovoltaic ferroelectrics [86]. The temperature-dependent measurement showed a significant decrease in SHG signal from 85 to 100 °C (Fig. 13a), indicating that a phase transition occurred. As depicted in Fig. 13b, the polarization (P)–electric field (E) hysteresis loop further confirmed the ferroelectricity of (R-/S-CHEA)PbI$_3$, where the small saturation polarization (P_s ~0.03 μC cm^{-2}) was ascribed to the low intrinsic polarization predicted by density functional theory and absence of alignment between the polarization and measurement axes [86]. Fig. 13c indicates the switchable diode effect of the ferroelectrics. Specifically, the photocurrent direction depends on the history of applied electric fields. A pre-positive bias will cause the diode with forward direction

toward the right in Fig. 13d, resulting in a negative photocurrent at zero bias. Further measurements demonstrated that the (*R-/S*-CHEA)PbI$_3$ underwent a ferroelectric-paraelectric phase transition at ~100 °C from the chiral–polar space group *P*2$_1$ to the chiral–nonpolar space group *P*2$_1$2$_1$2$_1$ [86].

In addition, H/F substitution (replacement of hydrogen atoms with fluorine atoms) may induce a minor structural disruption, thereby enhancing ferroelectric properties such as Curie temperature (*T*$_c$) and spontaneous polarization [176]. Some research groups designed a series of high *T*$_c$ molecular ferroelectrics by applying the strategy of H/F substitution in chiral HMHs [111,114,117]. Particularly, the (*R-/S*-FP)CdCl$_3$ (*R-/S*-FP = *R-/S*-3-fluoropyrrolidinium) ferroelectrics represent a pioneering example of combining H/F substitution and introducing chirality, in which the *T*$_c$ of (*R-/S*-FP)CdCl$_3$ was much higher (303 K) compared with the original (pyrrolidinium)CdCl$_3$ (240 K) [114,177]. Similarly, based on the prototype hybrid ferroelectric (pyrrolidinium)MnCl$_3$ [178], a striking increase by 38 K in *T*$_c$ proved the feasibility and importance of the strategy of H/F substitution (Fig. 13e) [111]. As shown in Fig. 13f, the (*R*- and *S*-FP)MnCl$_3$ exhibited comparable *P*$_s$ values, *i.e.*, ~5.0 and ~5.4 μC cm^{-2}, respectively. Furthermore, benefiting from the PL associated with octahedral Mn^{2+} ions, Gao et al. reported the CPL activity at room temperature from the (*R-/S*-FP)MnBr$_3$ molecular ferroelectrics [117]. They were crystallized in chiral–polar space group *P*2$_1$ at 223 K and chiral–nonpolar space group *C*222$_1$ at 293 K, corresponding to the ferroelectric and paraelectric phases, respectively. Also, the *P–E* hysteresis loop at 223 K further suggested the ferroelectric properties with *P*$_s$ values of 4.8 and 4.5 μC cm^{-2} for (*R*- and *S*-FP)MnBr$_3$, respectively [117].

5.3. Spintronics

5.3.1. Chiral-induced spin selectivity (CISS)

CISS effect was reported by Naaman et al., in 1999 [179], in which the electron transmission yield through chiral materials depends on the electron spin orientation. In other words, chiral materials can serve as electron spin filters [180,181]. Lu et al. investigated the spin-dependent charge transport in the thin films of chiral lead-free (*R-/S*-MBA)$_2$SnI$_4$ by means of magnetic conductive-probe atomic
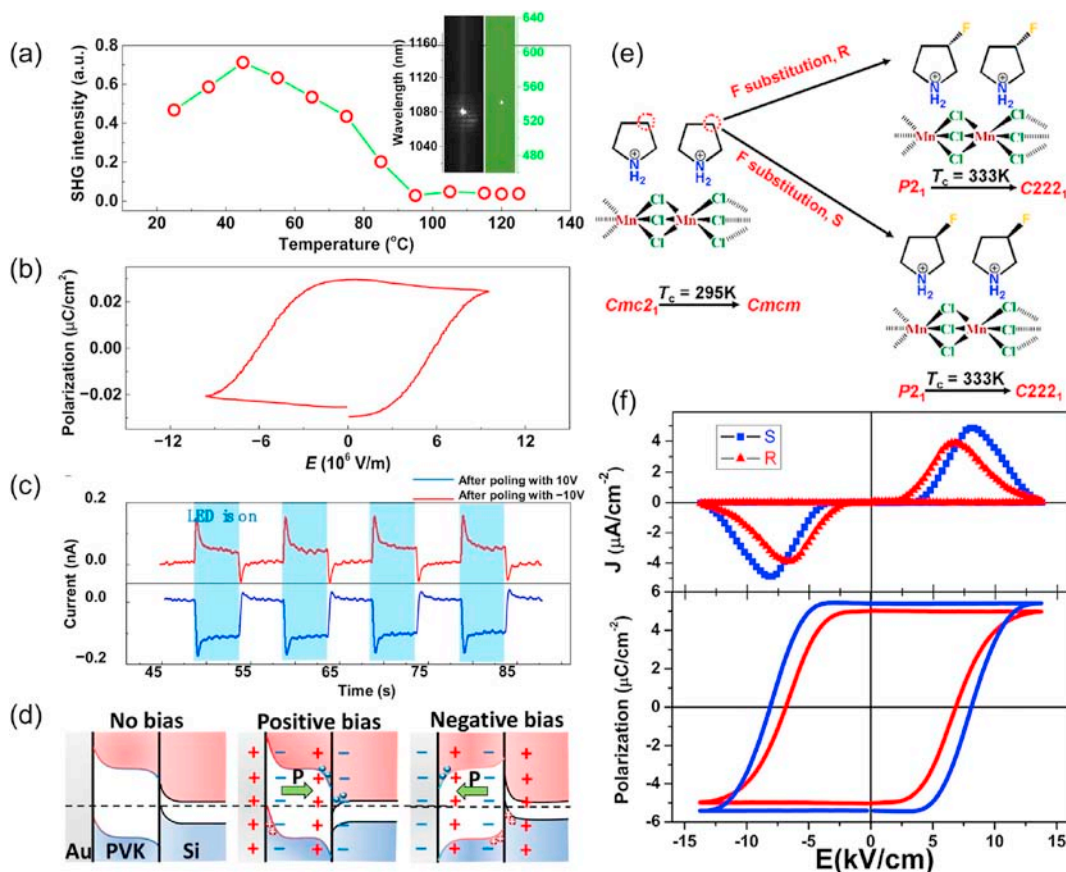

Fig. 13. Application of chiral HMHs as ferroelectrics. (a) SHG intensity as a function of temperature for the (*R-/S*-CHEA)PbI$_3$. Inset: SHG image excited with a 1080 nm infrared laser. (b) *P–E* hysteresis loop of the ferroelectrics (*R-/S*-CHEA)PbI$_3$. (c) Switchable diode effect in the chiral (*R-/S*-CHEA)PbI$_3$. (d) Band structure of the polycrystal device under zero bias, positive bias and negative bias. Reproduced with permission from Ref. [86]: Copyright 2020, American Association for the Advancement of Science. (e) Schematic design of molecular ferroelectrics by H/F substitution. (f) Ferroelectric hysteresis loops of (*R-/S*-FP)MnCl$_3$ measured along the polar *b*-axis at 313 K. Reproduced with permission from Ref. [111]: Copyright 2019, American Chemical Society.

force microscopy measurements [44]. The degree of spin polarization (P) is defined as:

$$P = \frac{I_+ - I_-}{I_+ + I_-} \times 100\% \tag{7}$$

where I_+ and I_- are the measured currents at -1 V when the tip magnetic field is pointing up or down, respectively. The average current–voltage (I–V) curves of chiral (R-/S-MBA)$_2$SnI$_4$ thin films with a thickness of 50–60 nm under the opposite magnetization directions were depicted in Fig. 14b. The P values of (R- and S-MBA)$_2$SnI$_4$ films were as high as +94% and −93%, respectively. The slight difference in spin-polarized current between lead- and tin-based chiral films indicated that spin-dephasing in the inorganic sublattice may not be significant [44,81]. Therefore, the spin-polarized current in chiral HMHs is mainly ascribed to the CISS effect of chiral organic molecules [99,128]. Generally, the CISS effect in chiral molecules is supposed to originate from a coupling between the linear momentum of an electron moving in a chiral potential and its spin, which can be expressed in Fig. 14a [182]. From the theoretical point of view, the CISS effect is associated with SOC [182,183]. Recently, Yu theoretically demonstrated that the spin-dependent charge transport in chiral HMHs can be traced to the chirality-induced SOC [184]. The SOC describes a relativistic effect, which can be
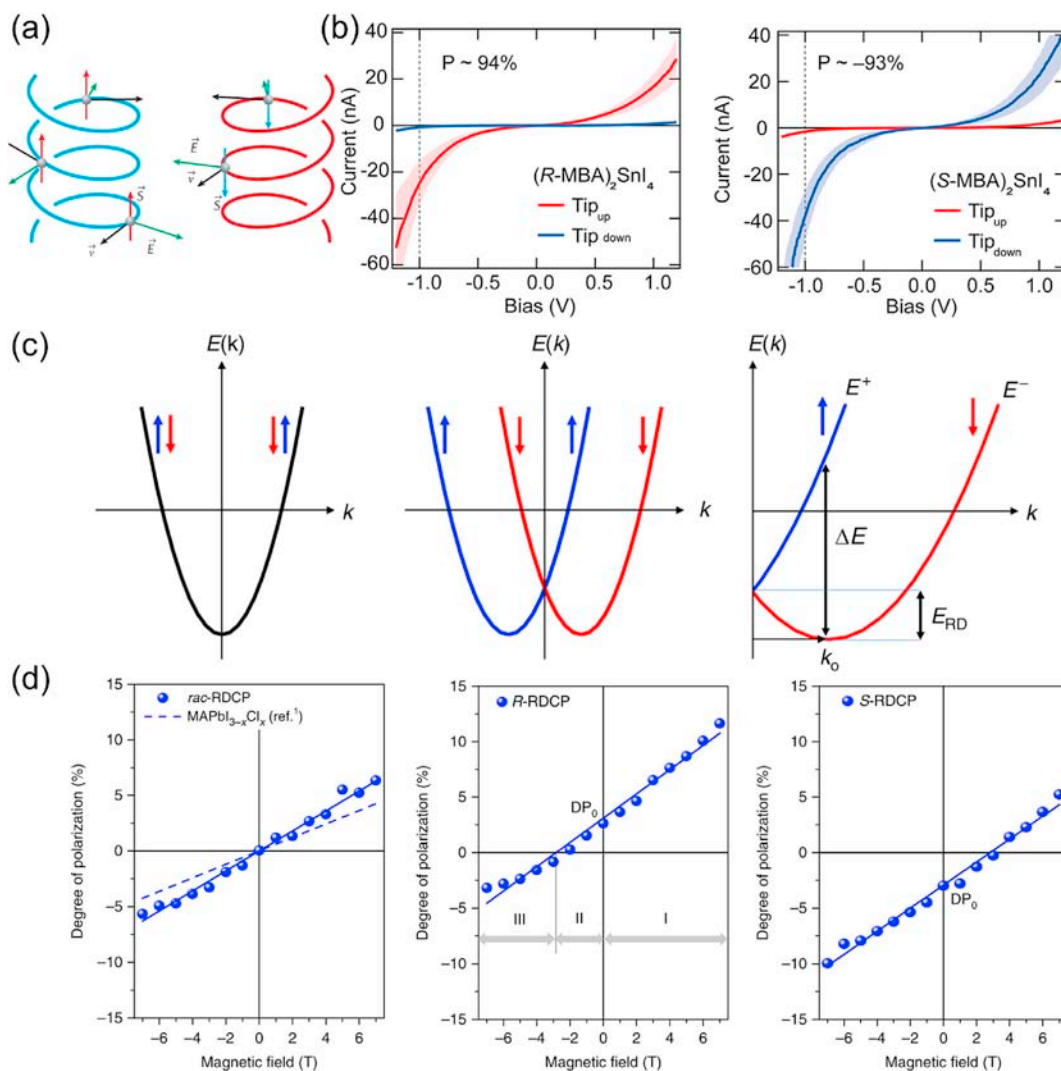

Fig. 14. (a) Schematic of spins spiralling along chiral molecules with different handedness. Reproduced with permission from Ref. [183]: Copyright 2021, Springer Nature. (b) I–V curves of chiral 2D (R-/S-MBA)$_2$SnI$_4$ thin films at room-temperature. Reproduced with permission from Ref. [44]: Copyright 2020, American Chemical Society. (c) Schematic diagram of the two-fold spin-degenerate electronic band in a conventional semiconductor and the separated spin-polarized sub-bands in k-space. ΔE is the energy difference at the characteristic momentum (k_0) between the inner and outer spin-polarized branches produced by the Rashba-Dresselhaus spin-splitting. E_{RD} is the characteristic Rashba-Dresselhaus energy. Reproduced with permission from Ref. [19]: Copyright 2020, Springer Nature. (d) DP for chiral and achiral quasi-2D HMHs with applied magnetic field varied from −7 T to 7 T. Reproduced with permission from Ref. [60]: Copyright 2018, Springer Nature.

expressed as the Zeeman-like interaction between the electron spin and an effective magnetic field transformed by the electric field experienced by a moving electron in its rest frame [185].

5.3.2. Rashba-Dresselhaus SOC effects

In non-magnetic systems, the SOC maintains time-reversal symmetry and the "up" and "down" of two electronic spin states are degenerate [19]. The spin degeneracy is broken in chiral materials on account of the effective magnetic field generated by the electron velocity coupling with the chiral electrical potential, resulting in the splitting of the two electronic spin state energies [180]. The phenomenon of spin-splitting by generating an effective magnetic field is known as Rashba or Dresselhaus effect [186,187], which can occur either exclusively or simultaneously in materials distinguished by the characteristics of the site or bulk inversion asymmetry, respectively
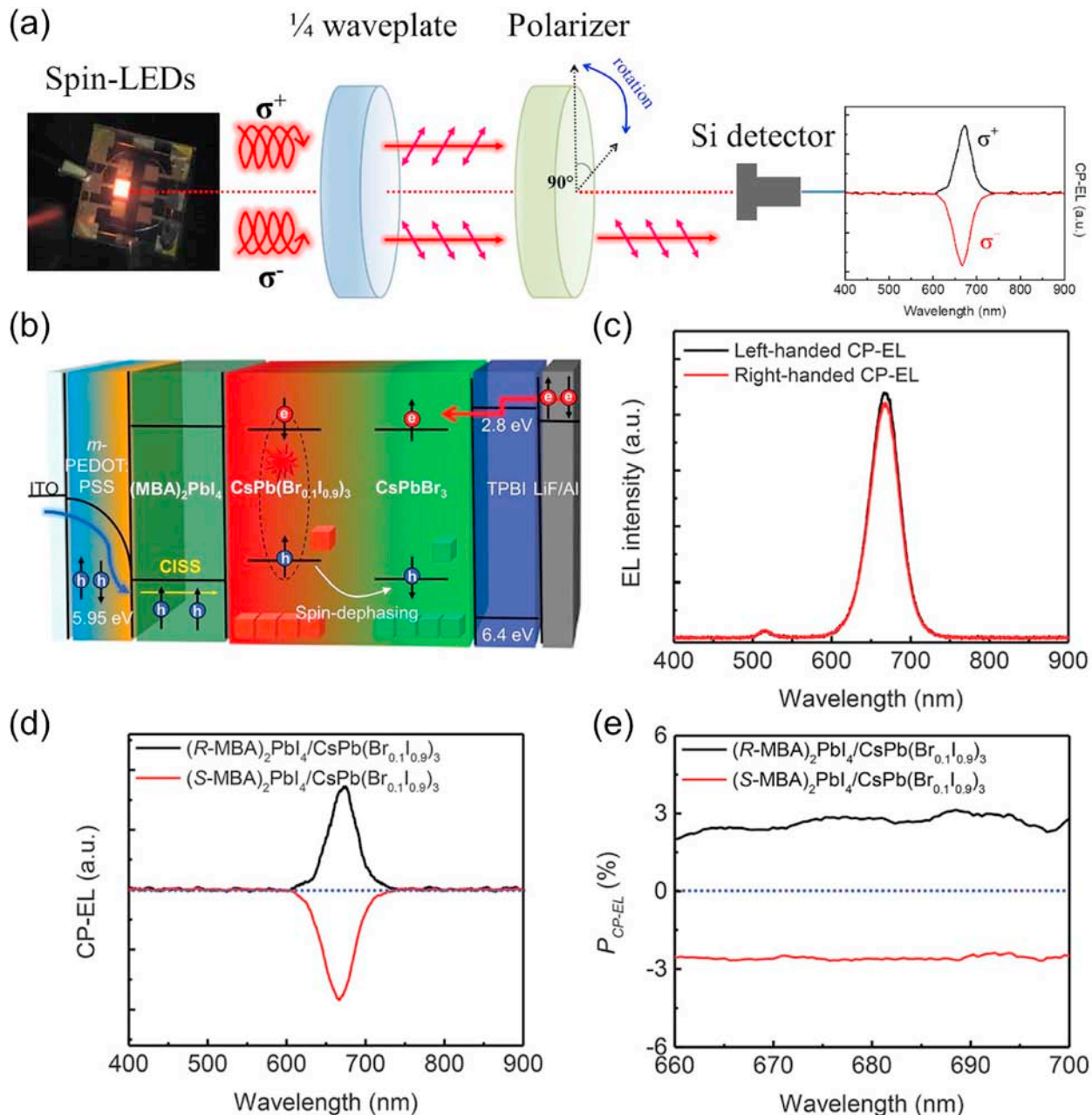

Fig. 15. Application of chiral HMHs as spin-LEDs. (a) Schematic illustration of CPEL measurement system. (b) Schematic diagram of the generation of CPEL in the spin-LEDs. (c) Left- and right-handed CPEL spectra of the spin-LEDs based on $(R\text{-}/S\text{-MBA})_2PbI_4/CsPbBr_3$ heterostructure. (d) CPEL spectra of $(R\text{-}/S\text{-MBA})_2PbI_4/CsPbBr_3$-based device. (e) DP as a function of wavelength for the spin-LEDs based on CISS layer/$CsPbBr_3$ heterostructure. Reproduced with permission from Ref. [20]: Copyright 2021, American Association for the Advancement of Science.

[188]. Based on hybrid density-functional theory calculations, Jana et al. demonstrated that the Rashba-Dresselhaus spin-splitting of electronic band structures in chiral HMHs is a consequence of chirality-induced inversion asymmetry [19]. In short, the spin-polarized sub-bands are separated in k-space on account of the SOC and inversion asymmetry of the Rashba-Dresselhaus semiconductor, as illustrated in Fig. 14c. Furthermore, the spin degeneracy is broken in chiral HMHs, leading to the spin-polarized absorption (induced CD) and spin-polarized PL, without employing a magnetic field or circularly polarized light excitation to generate spin-polarized carriers. For example, Long et al. reported spin polarization control in quasi-2D HMHs through chemical design and by a magnetic field, and both spin-polarized absorption and PL were demonstrated [60]. As shown in Fig. 14d, the averaged DP at 2 K under LCP and RCP light excitation was achieved to be ~3% for both thin films of chiral quasi-2D HMHs at 0 T, which was comparable to the value of ~3% for 3D $MAPbI_{3-x}Cl_x$ at 5 T [189]. Moreover, the spin polarization can be further controlled by the applied external magnetic field.

5.3.3. Spin light-emitting diodes (LEDs)

LCP or RCP emission can be generated when the population of carriers (n) is spin-polarized (*i.e.*, spin "up" > "down", or vice versa). The CISS effect of chiral HMHs enables the producing of the spin-polarized current by applying an electric field. Using the poly-crystalline thin films of chiral (R-/S-MBA)$_2$PbI$_4$ with a thickness of 30–60 nm as the spin-polarized hole injection layer, Kim et al. fabricated spin-LEDs based on the heterostructure of chiral HMHs/perovskite nanocrystals [20]. Fig. 15a depicts the schematic diagram for the measurement of circularly polarized electroluminescence (CPEL) for the spin-LEDs. During the generation of CPEL, the spin-polarized holes were injected into the adjacent perovskite emitting layer (Fig. 15b). Additionally, a halide exchange occurred near the HMHs-perovskite interface, eventually resulting in two emission peaks at 678 and 515 nm from CsPb(Br$_{0.1}$I$_{0.9}$)$_3$ and CsPbBr$_3$, respectively (Fig. 15c). However, CPEL was not observed at 515 nm, as a result of additional spin dephasing and scattering of the spin-polarized holes outside the HMHs-perovskite interface [20], as shown in Fig. 15d. Importantly, when the CsPbI$_3$ and CsPb(Br$_{0.1}$I$_{0.9}$)$_3$ nanocrystalline films were used as the emitting layers, the average DP values at room temperature were determined as $\pm$ 0.25% and $\pm$2.6%, respectively (Fig. 15e). In addition, it was demonstrated that the spin-LEDs based on CsPb(Br$_{0.1}$I$_{0.9}$)$_3$ nanocrystals exhibited enhanced CPEL [20].

5.3.4. Magneto-optical detection

As mentioned above, the CISS effect can be externalized through magnetic conductive-probe atomic force microscopic measurements. In relation to the CISS effect, Huang et al. developed an all-optical excitation and measurement scheme [87]. In the manufactured
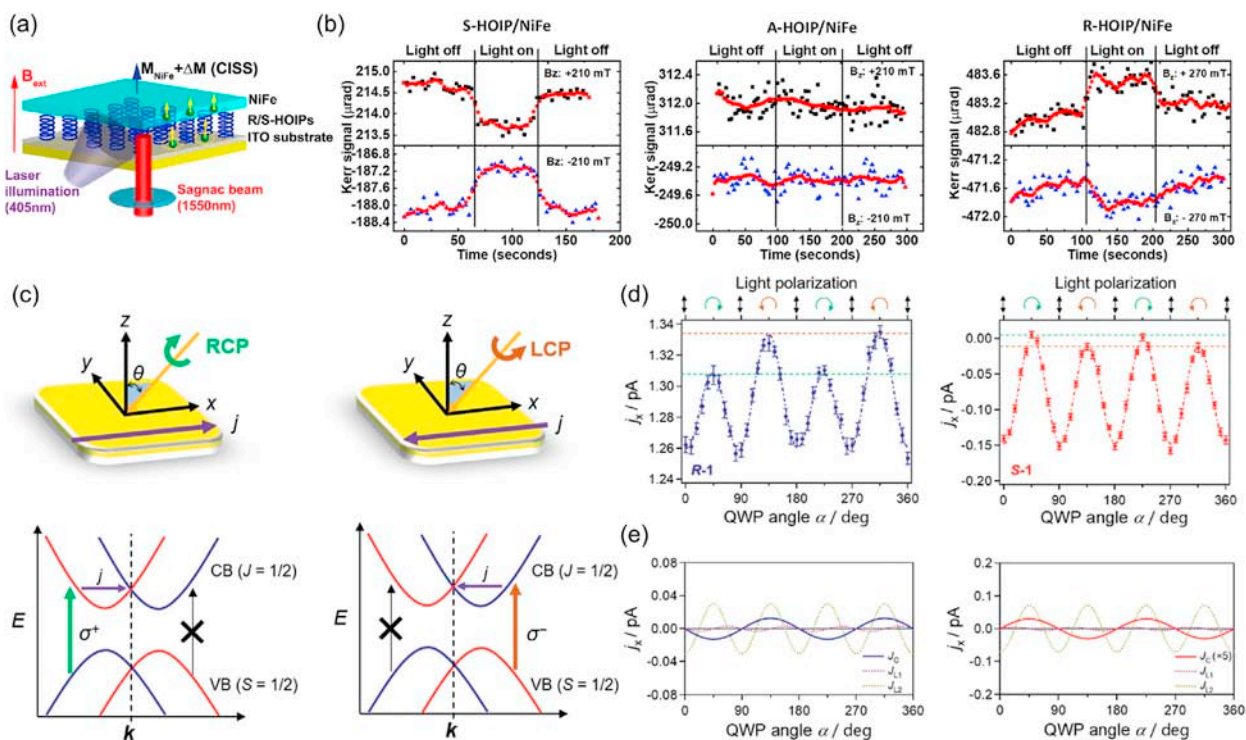

Fig. 16. (a) Schematic illustration of the Sagnac magneto-optical Kerr effect for the photoinduced magnetization at chiral HMHs/NiFe interface. (b) The change in Kerr signal upon photoexcitation for chiral and achiral HMHs/NiFe samples under positive and negative out-of-plane external magnetic field, respectively. Reproduced with permission from Ref. [87]: Copyright 2020, American Chemical Society. (c) Schematic diagram of photocurrent generation by CPGE in a semiconductor. (d) Photocurrent (J_x) as a function of the angle (α) of the $\lambda/4$ waveplate (QWP). (e) Contributions of light-helicity-dependent photocurrent J_C, and light-helicity-independent photocurrents J_{L1} and J_{L2} to the total photocurrent in chiral (R-/S-BPEA)$_2$PbI$_4$. Reproduced with permission from Ref. [94]: Copyright 2021, John Wiley and Sons.

chiral HMHs and ferromagnetic NiFe heterostructures, the magneto-optical Kerr effect with sensitivity to small amounts of spin accumulation was employed to examined CISS-related behaviors through a Sagnac interferometer (Fig. 16a). As a result of the opto-electronic response and CISS effect of chiral HMHs, the time evolution of the Kerr angle of the chiral samples irradiated at 405 nm showed distinct signals and chirality correlation in different external magnetic field directions, whereas achiral samples exhibited no significant changes in the Kerr signal upon photoexcitation, as described in Fig. 16b. Since the photocurrent generated in the chiral films was spin-polarized, the magnetization produced by photoexcitation at the NiFe surface (*i.e.*, the extra Kerr signal) increased the magnetization of the NiFe film and the sign of the spin polarization showed chirality correlation [87]. This work demonstrated that magneto-optical detection provided an alternative approach to investigate the CISS effect of chiral HMHs, opening the way for the next-generation chiral spintronics.
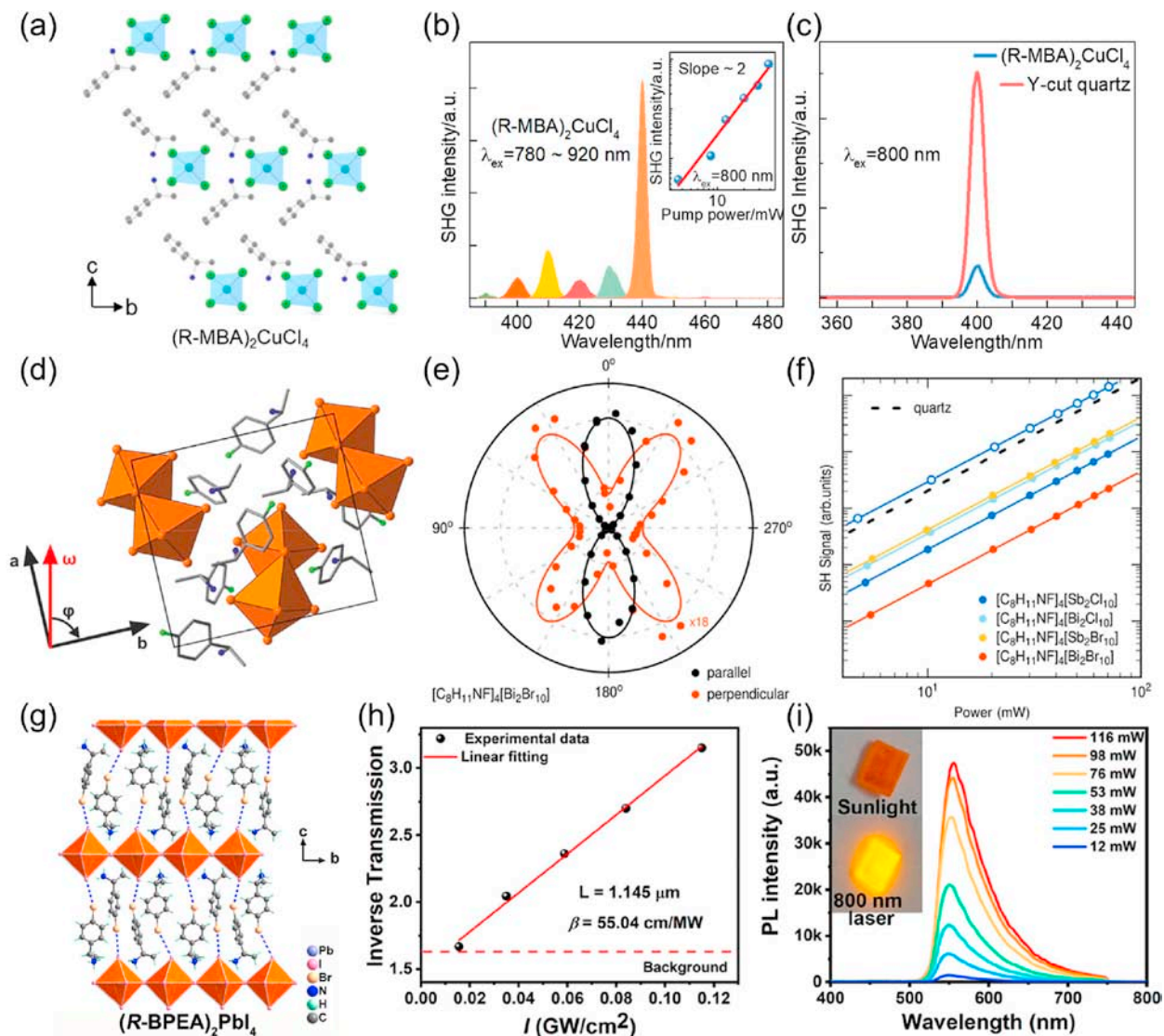

Fig. 17. Application of chiral HMHs in nonlinear optics. (a) Crystal structure of the chiral $(R\text{-MBA})_2\text{CuCl}_4$. (b) Wavelength-dependent SHG signals of the chiral $(R\text{-MBA})_2\text{CuCl}_4$. Inset: Plot of SHG intensity versus pump power. (c) Comparison of SHG intensities between the chiral $(R\text{-MBA})_2\text{CuCl}_4$ and a Y-cut quartz reference. Reproduced with permission from Ref. [64]: Copyright 2021, John Wiley and Sons. (d) Top view of the crystal structure of $(R\text{-FPEA})_4\text{Sb}_2\text{Cl}_{10}$ viewed along the *c*-axis. (e) Polar plot of the SHG intensity as a function of the crystal azimuth angle. (f) SHG signal versus applied laser power for the $(R\text{-FPEA})_4\text{E}_2\text{X}_{10}$ (E = Sb and Bi, X = Cl and Br) compounds compared with a quartz reference. Reproduced with permission from Ref. [85]: Copyright 2020, American Chemical Society. (g) Stacked crystal structures of $(R\text{-BPEA})_2\text{PbI}_4$. (h) Inverse transmission versus incident laser peak intensity for $(R\text{-BPEA})_2\text{PbI}_4$. (i) The corresponding excitation intensity-dependent PL spectra at 800 nm. Inset: Photographs of $(R\text{-BPEA})_2\text{PbI}_4$ under sunlight and 800 nm laser irradiation. Reproduced with permission from Ref. [100]: Copyright 2021, American Chemical Society.

5.3.5. Circular photogalvanic effect (CPGE)

As an exciting spin-related optoelectronic phenomenon, CPGE arises from the SOC of non-centrosymmetric systems. It describes the generation of photocurrent sensitive to the photon helicity of the excitation light under the irradiation of circularly polarized light when there is no bias voltage [190]. The SOC-induced spin-splitting of electronic band structures would bring about selective inter-band excitation of electron in a momentum space (*k*-space) under the excitation of circularly polarized light, as shown in Fig. 16c. To date, Vardeny and Miyasaka et al. successively reported the CPGE in chiral HMHs [94,96]. Among the 11 pairs of enantiomorphic space groups, the first example of crystallization in chiral space groups $P4_32_12$ and $P4_12_12$, $(R\text{-}/S\text{-}BPEA)_2PbI_4$ ($R\text{-}/S\text{-}BPEA = R\text{-}/S\text{-}1\text{-}(4\text{-bromophenyl})ethylammonium$) was employed to study CPGE by Miyasaka et al. [94]. As illustrated in Fig. 16d, the photocurrents of both $(R\text{-}/S\text{-}BPEA)_2PbI_4$ differ a lot under the excitation of RCP and LCP light, as a result of CPGE. The photocurrent decomposition was depicted in Fig. 16e. Because the CPGE-induced photocurrent (J_C) from the surface should have the same sign, its direction should not be influenced by the surface-polarity. Instead, the J_C direction depends on the chirality of the samples, which can be attributed to the spin-polarized electronic band structures in different chiral samples [94,191].

5.4. Nonlinear optics

Nonlinear optics describes the interaction between light and matter under strong coherent light [192–195]. In such case, the nonlinear polarization (***P***) of media can be interpreted as a function of the electric field (***E***), which is calculated as [196]:

$$P = \varepsilon_0\left(\chi^{(1)}E + \chi^{(2)}E^2 + \chi^{(3)}E^3 + \cdots\right) \tag{8}$$

where ε_0 is vacuum permittivity, $\chi^{(n)}$ is the n-th order electric susceptibility. Particularly, even-order NLO responses, such as SHG, require strictly non-centrosymmetric structures. However, traditional HMHs are crystallized in centrosymmetric space groups, in which no efficient SHG signals can be observed [197]. Although surface asymmetry may cause weak SHG in traditional HMHs, strong SHG can only be obtained in chiral HMHs with broken inversion symmetry.

Yuan et al. studied the SHG in the nanowires of chiral HMHs [130], and our group subsequently demonstrated efficient SHG in the chiral $(R\text{-}MBA)_2CuCl_4$ thin films with their crystal structures presented in Fig. 17a [64]. The latter exhibited efficient SHG signals in a wide wavelength range of 780–920 nm, as illustrated in Fig. 17b. In addition, the effective SHG coefficient of chiral $(R\text{-}MBA)_2CuCl_4$ thin film at 800 nm was roughly evaluated as 0.35 p.m. V^{-1} using Y-cut quartz as a reference with the optimized linearly polarized pump light (Fig. 17c). In addition, Dehnhardt et al. characterized the rotational anisotropy of SHG intensity along the *c*-axis in the single crystals of chiral $(R\text{-}FPEA)_4Sb_2Cl_{10}$ ($R\text{-}FPEA = R\text{-}1\text{-}(4\text{-fluoro})\text{-phenylethylammonium}$) (Fig. 17d) [85]. As shown in Fig. 17e, for the chiral lead-free HMHs, *i.e.*, $(R\text{-}FPEA)_4E_2X_{10}$ (E = Sb and Bi, X = Cl and Br), the polarization-dependent rotational anisotropy was consistent with the expectation of $P2_1$ space group and SHG signals were almost comparable to that of Z-cut quartz (Fig. 17f) [85]. Very recently, efficient SHG signals were observed in the single crystals of chiral 1D $(R\text{-}/S\text{-}APD)PbI_4$ ($R\text{-}/S\text{-}APD = R\text{-}/S\text{-}3\text{-aminopiperidinium}$) and 0D $(R\text{-}/S\text{-}MPEA)_2SnBr_6$ [101,127]. Furthermore, SHG effect, which is sensitive to inversion symmetry, can be employed as a powerful method to study the phase transition of ferroelectric materials.

It should be noted that chiral HHMs should also be one kind of novel materials with excellent two-photon absorption (TPA) properties. As shown in Fig. 17g–i, Luo et al. determined the TPA coefficient of chiral $(R\text{-}BPEA)_2PbI_4$ single crystal as 55.04 cm MW^{-1}, which is almost the highest value among 2D HMHs [100]. Thanks to the large TPA, the single crystal can be used for dual-modal direct detection of circularly polarized light at 520 and 800 nm. Owing to the excellent photoresponse ability and large TPA coefficient, the photocurrent anisotropy factor was higher than 0.1 [100]. Very recently, Zhao et al. synthesized highly ordered microwire arrays of chiral $(R\text{-}/S\text{-}CPEA)_2PbI_4$, which demonstrated both SHG and TPA with large anisotropy under linearly polarized excitation at 800 nm [198]. Although there are only several papers reporting the TPA properties of chiral HMHs, we believe it will be a topic worthy of further study.

6. Summary and outlook

Chiral HMHs, as a newly flourishing type of chiral semiconductor materials, have been greatly developed over the past few years. The introduction of chirality into HMHs endows them with fascinating and exciting chirality-related optoelectronic properties, and creates promising and exclusive platform for chiral optoelectronics. Herein, we comprehensively reviewed the research progress in single crystals and thin films of chiral HMHs, including diverse structural frameworks, synthetic methods, fundamental physics and strategies for the modulation of optical activity, as well as the related optoelectronic applications. Because the research on single crystals and thin films of chiral HMHs is still in its infancy, there are still plenty of new challenges and opportunities to be addressed in the future, which are summarized and highlighted as follows.

1) Design and synthesis strategies. The design and synthesis of novel chiral HMHs are a prerequisite for comprehensively exploring their intrinsic characteristics and exploiting potential applications. First, chiral 3D HMHs possess low exciton binding energy and long carrier diffusion lengths, suggesting their promising applications in high-performance chiral optoelectronic devices. Although Long et al. made theoretical predictions on 3D chiral HMHs [53], synthesizing 3D HMHs still remains a challenge. Secondly, it is meaningful to develop more chiral HMHs with the bulky and interchangeable chiral organic components on the basis of existing material synthesis. More materials with various special functionalities, such as achiral structure [115], crystal–glass transition [95], ferromagnetism [91,126], ferroelasticity [123], piezoelectricity [124], or morphology variability [130,165,199], should be explored

and studied to enrich the family of chiral HMHs and further understand their structure–property relationships. Thirdly, the development of theoretical design principle (discussed in Section 4.1.2) and new synthetic strategies, as well as the optimization of the synthesis process (discussed in Section 3), should be implemented consistently, which are essential for the enhancement of chirality in HMHs and realization of relevant applications. Lastly, the current optoelectronic applications are based on toxic lead-based chiral HMHs. Therefore, it is also an important and urgent task to develop lead-free chiral HMHs materials for their applications in optoelectronic devices.

2) Ultrafast carrier dynamics in chiral HMHs. Although the CD and CPL of various chiral HMHs have been intensively investigated, the study on the ultrafast carrier dynamics still lag far behind. The deep understanding on the carrier dynamics in chiral HMHs is vital for further exploration of their relevant applications. For example, by means of ultrafast pump-probe spectrum [200], Xiong et al. investigated transient CD and exciton spin dynamics in $CsPbBr_3$, which provided important information for the realization of spintronic applications [201]. Similarly, as described in Section 5.3.1, the CISS effect in chiral HMHs is considered to be associated with the chirality-induced SOC, *i.e.*, Rashba or Dresselhaus SOC, and thus leads to spin splitting in chiral HMHs. Obviously, the study on the carrier dynamics process is vital to reveal the impact of Rashba or Dresselhaus SOC.

3) Broadening of optoelectronic applications. Although various optoelectronic devices based on chiral HMMs have been developed, it is still of great significance to further broaden their applications. Single crystals and thin films not only afford a versatile platform for understanding the intrinsic properties of chiral HMHs, but also lay the foundation for further exploration of their optoelectronic applications. For example, some spin-related phenomena and applications have not been fully exploited, such as CPGE. Also, there are only several examples of chiral ferroelectrics, and the development of multifunctional chiral ferroelectric materials is imminent. Furthermore, as a result of intrinsic asymmetry of chiral materials and highly flexible tunability of structure, the chiral HMHs may be a novel type of NLO materials with great application prospect. It will be an interesting and challenging topic to reveal the relationship between material structure (space group) and NLO properties, including SHG and TPA.

Acknowledgements

References

[1] J.A. Schellman, Symmetry rules for optical rotation, J. Chem. Phys. 44 (1966) 55–63.
[2] Y. Wang, J. Xu, Y. Wang, H. Chen, Emerging chirality in nanoscience, Chem. Soc. Rev. 42 (2013) 2930–2962.
[3] Y. Zhao, A.N. Askarpour, L. Sun, J. Shi, X. Li, A. Alù, Chirality detection of enantiomers using twisted optical metamaterials, Nat. Commun. 8 (2017), 14180.
[4] J.Y.C. Lim, I. Marques, V. Félix, P.D. Beer, A chiral halogen-bonding [3]rotaxane for the recognition and sensing of biologically relevant dicarboxylate anions, Angew. Chem. Int. Ed. 57 (2018) 584–588.
[5] C. Hao, A. Qu, L. Xu, M. Sun, H. Zhang, C. Xu, H. Kuang, Chiral molecule-mediated porous Cu_xO nanoparticle clusters with antioxidation activity for ameliorating Parkinson's disease, J. Am. Chem. Soc. 141 (2019) 1091–1099.
[6] S. Yoo, Q.H. Park, Metamaterials and chiral sensing: a review of fundamentals and applications, Nanophotonics 8 (2019) 249–261.
[7] Y. Zhao, C. Xu, DNA-based plasmonic heterogeneous nanostructures: building, optical responses, and bioapplications, Adv. Mater. 32 (2020), 1907880.
[8] M. Sun, A. Qu, C. Hao, X. Wu, L. Xu, C. Xu, H. Kuang, Chiral upconversion heterodimers for quantitative analysis and bioimaging of antibiotic-resistant bacteria in vivo, Adv. Mater. 30 (2018), 1804241.
[9] C. Hao, X. Wu, M. Sun, H. Zhang, A. Yuan, L. Xu, C. Xu, H. Kuang, Chiral core–shell upconversion nanoparticle@MOF nanoassemblies for quantification and bioimaging of reactive oxygen species in vivo, J. Am. Chem. Soc. 141 (2019) 19373–19378.
[10] Z. Cao, H. Gao, M. Qiu, W. Jin, S. Deng, K.-Y. Wong, D. Lei, Chirality transfer from sub-nanometer biochemical molecules to sub-micrometer plasmonic metastructures: physiochemical mechanisms, biosensing, and bioimaging opportunities, Adv. Mater. 32 (2020), 1907151.
[11] J. Cheng, J. Hao, H. Liu, J. Li, J. Li, X. Zhu, X. Lin, K. Wang, T. He, Optically active CdSe-dot/CdS-rod nanocrystals with induced chirality and circularly polarized luminescence, ACS Nano 12 (2018) 5341–5350.
[12] Y. Li, J. Cheng, J. Li, X. Zhu, T. He, R. Chen, Z. Tang, Tunable chiroptical properties from the plasmonic band to metal-ligand charge transfer band of cysteine-capped molybdenum oxide nanoparticles, Angew. Chem. Int. Ed. 57 (2018) 10236–10240.
[13] B. Zhao, H. Yu, K. Pan, Z.a. Tan, J. Deng, Multifarious chiral nanoarchitectures serving as handed-selective fluorescence filters for generating full-color circularly polarized luminescence, ACS Nano 14 (2020) 3208–3218.
[14] Y. Sang, J. Han, T. Zhao, P. Duan, M. Liu, Circularly polarized luminescence in nanoassemblies: generation, amplification, and application, Adv. Mater. 32 (2020), 1900110.
[15] D. Di Nuzzo, L. Cui, J.L. Greenfield, B. Zhao, R.H. Friend, S.C.J. Meskers, Circularly polarized photoluminescence from chiral perovskite thin films at room temperature, ACS Nano 14 (2020) 7610–7616.
[16] F. Zinna, G. Albano, A. Taddeucci, T. Colli, L.A. Aronica, G. Pescitelli, L. Di Bari, Emergent nonreciprocal circularly polarized emission from an organic thin film, Adv. Mater. 32 (2020), 2002575.
[17] S. Jiang, M. Chekini, Z.-B. Qu, Y. Wang, A. Yeltik, Y. Liu, A. Kotlyar, T. Zhang, B. Li, H.V. Demir, Chiral ceramic nanoparticles and peptide catalysis, J. Am. Chem. Soc. 139 (2017) 13701–13712.
[18] J. Yeom, U.S. Santos, M. Chekini, M. Cha, A.F. de Moura, N.A. Kotov, Chiromagnetic nanoparticles and gels, Science 359 (2018) 309–314.
[19] M.K. Jana, R. Song, H. Liu, D.R. Khanal, S.M. Janke, R. Zhao, C. Liu, Z. Valy Vardeny, V. Blum, D.B. Mitzi, Organic-to-inorganic structural chirality transfer in a 2D hybrid perovskite and impact on Rashba-Dresselhaus spin-orbit coupling, Nat. Commun. 11 (2020) 4699.
[20] Y.-H. Kim, Y. Zhai, H. Lu, X. Pan, C. Xiao, E.A. Gaulding, S.P. Harvey, J.J. Berry, Z.V. Vardeny, J.M. Luther, M.C. Beard, Chiral-induced spin selectivity enables a room-temperature spin light-emitting diode, Science 371 (2021) 1129–1133.
[21] A. Kojima, K. Teshima, Y. Shirai, T. Miyasaka, Organometal halide perovskites as visible-light sensitizers for photovoltaic cells, J. Am. Chem. Soc. 131 (2009) 6050–6051.
[22] A.K. Jena, A. Kulkarni, T. Miyasaka, Halide perovskite photovoltaics: background, status, and future prospects, Chem. Rev. 119 (2019) 3036–3103.
[23] L. Lin, T.W. Jones, T.C.-J. Yang, N.W. Duffy, J. Li, L. Zhao, B. Chi, X. Wang, G.J. Wilson, Inorganic electron transport materials in perovskite solar cells, Adv. Funct. Mater. 31 (2021), 2008300.
[24] L.N. Quan, B.P. Rand, R.H. Friend, S.G. Mhaisalkar, T.-W. Lee, E.H. Sargent, Perovskites for next-generation optical sources, Chem. Rev. 119 (2019) 7444–7477.

[25] L. Kong, X. Zhang, Y. Li, H. Wang, Y. Jiang, S. Wang, M. You, C. Zhang, T. Zhang, S.V. Kershaw, W. Zheng, Y. Yang, Q. Lin, M. Yuan, A.L. Rogach, X. Yang, Smoothing the energy transfer pathway in quasi-2D perovskite films using methanesulfonate leads to highly efficient light-emitting devices, Nat. Commun. 12 (2021) 1246.

[26] H. Wang, X. Gong, D. Zhao, Y.-B. Zhao, S. Wang, J. Zhang, L. Kong, B. Wei, R. Quintero-Bermudez, O. Voznyy, Y. Shang, Z. Ning, Y. Yan, E.H. Sargent, X. Yang, A multi-functional molecular modifier enabling efficient large-area perovskite light-emitting diodes, Joule 4 (2020) 1977–1987.

[27] H. Wang, X. Zhang, Q. Wu, F. Cao, D. Yang, Y. Shang, Z. Ning, W. Zhang, W. Zheng, Y. Yan, S.V. Kershaw, L. Zhang, A.L. Rogach, X. Yang, Trifluoroacetate induced small-grained CsPbBr$_3$ perovskite films result in efficient and stable light-emitting devices, Nat. Commun. 10 (2019) 665.

[28] D. Shi, V. Adinolfi, R. Comin, M. Yuan, E. Alarousu, A. Buin, Y. Chen, S. Hoogland, A. Rothenberger, K. Katsiev, Y. Losovyj, X. Zhang, P.A. Dowben, O.F. Mohammed, E.H. Sargent, O.M. Bakr, Low trap-state density and long carrier diffusion in organolead trihalide perovskite single crystals, Science 347 (2015) 519–522.

[29] F. Huang, M. Li, P. Siffalovic, G. Cao, J. Tian, From scalable solution fabrication of perovskite films towards commercialization of solar cells, Energy Environ. Sci. 12 (2019) 518–549.

[30] Y. Dong, Y. Zhang, X. Li, Y. Feng, H. Zhang, J. Xu, Chiral perovskites: promising materials toward next-generation optoelectronics, Small 15 (2019), 1902237.

[31] G. Long, R. Sabatini, M.I. Saidaminov, G. Lakhwani, A. Rasmita, X. Liu, E.H. Sargent, W. Gao, Chiral-perovskite optoelectronics, Nat. Rev. Mater. 5 (2020) 423–439.

[32] Y. Dang, X. Liu, B. Cao, X. Tao, Chiral halide perovskite crystals for optoelectronic applications, Matter 4 (2021) 794–820.

[33] S. Ma, J. Ahn, J. Moon, Chiral perovskites for next-generation photonics: from chirality transfer to chiroptical activity, Adv. Mater. 33 (2021), 2005760.

[34] J. Ma, H. Wang, D. Li, Recent progress of chiral perovskites: materials, synthesis, and properties, Adv. Mater. 33 (2021), 2008785.

[35] Q.A. Akkerman, L. Manna, What defines a halide perovskite? ACS Energy Lett. 5 (2020) 604–610.

[36] V.A. Kuznetsova, E. Mates-Torres, N. Prochukhan, M. Marcastel, F. Purcell-Milton, J. O'Brien, A.K. Visheratina, M. Martinez-Carmona, Y. Gromova, M. Garcia-Melchor, Effect of chiral ligand concentration and binding mode on chiroptical activity of CdSe/CdS quantum dots, ACS Nano 13 (2019) 13560–13572.

[37] J. Hao, Y. Li, J. Miao, R. Liu, J. Li, H. Liu, Q. Wang, H. Liu, M.-H. Delville, T. He, K. Wang, X. Zhu, J. Cheng, Ligand-induced chirality in asymmetric CdSe/CdS nanostructures: a close look at chiral tadpoles, ACS Nano 14 (2020) 10346–10358.

[38] F. Li, Y. Li, X. Yang, X. Han, Y. Jiao, T. Wei, D. Yang, H. Xu, G. Nie, Highly fluorescent chiral N-S-doped carbon dots from cysteine: affecting cellular energy metabolism, Angew. Chem. Int. Ed. 57 (2018) 2377–2382.

[39] M. Zhang, L. Hu, H. Wang, Y. Song, Y. Liu, H. Li, M. Shao, H. Huang, Z. Kang, One-step hydrothermal synthesis of chiral carbon dots and their effects on mung bean plant growth, Nanoscale 10 (2018) 12734–12742.

[40] L. Xiao, T. An, L. Wang, X. Xu, H. Sun, Novel properties and applications of chiral inorganic nanostructures, Nano Today 30 (2020), 100824.

[41] Y. Shi, P. Duan, S. Huo, Y. Li, M. Liu, Endowing perovskite nanocrystals with circularly polarized luminescence, Adv. Mater. 30 (2018), 1705011.

[42] P. Liu, W. Chen, Y. Okazaki, Y. Battie, L. Brocard, M. Decossas, E. Pouget, P. Müller-Buschbaum, B. Kauffmann, S. Pathan, T. Sagawa, R. Oda, Optically active perovskite CsPbBr$_3$ nanocrystals helically arranged on inorganic silica nanohelices, Nano Lett. 20 (2020) 8453–8460.

[43] J. Ahn, S. Ma, J.-Y. Kim, J. Kyhm, W. Yang, J.A. Lim, N.A. Kotov, J. Moon, Chiral 2D organic inorganic hybrid perovskite with circular dichroism tunable over wide wavelength range, J. Am. Chem. Soc. 142 (2020) 4206–4212.

[44] H. Lu, C. Xiao, R. Song, T. Li, A.E. Maughan, A. Levin, R. Brunecky, J.J. Berry, D.B. Mitzi, V. Blum, M.C. Beard, Highly distorted chiral two-dimensional tin iodide perovskites for spin polarized charge transport, J. Am. Chem. Soc. 142 (2020) 13030–13040.

[45] D.G. Billing, A. Lemmerer, Bis[(S)-[β]-phenethylammonium] tribromoplumbate(II), Acta Crystallogr. 59 (2003) m381–m383.

[46] D.G. Billing, A. Lemmerer, Synthesis and crystal structures of inorganic–organic hybrids incorporating an aromatic amine with a chiral functional group, CrystEngComm 8 (2006) 686–695.

[47] J. Ahn, E. Lee, J. Tan, W. Yang, B. Kim, J. Moon, A new class of chiral semiconductors: chiral-organic-molecule-incorporating organic-inorganic hybrid perovskites, Mater. Horiz. 4 (2017) 851–856.

[48] H.D. Flack, Chiral and achiral crystal structures, Helv. Chim. Acta 86 (2003) 905–921.

[49] L. Sohncke, Entwickelung einer Theorie der Krystallstruktur, BG Teubner, 1879.

[50] M.V. Hobden, Optical activity in a non-enantiomorphous single gallium sulphide, Nature 216 (1967), 678-678.

[51] K. Claborn, C. Isborn, W. Kaminsky, B. Kahr, Optical rotation of achiral compounds, Angew. Chem. Int. Ed. 47 (2008) 5706–5717.

[52] P.S. Halasyamani, K.R. Poeppelmeier, Noncentrosymmetric oxides, Chem. Mater. 10 (1998) 2753–2769.

[53] G. Long, Y. Zhou, M. Zhang, R. Sabatini, A. Rasmita, L. Huang, G. Lakhwani, W. Gao, Theoretical prediction of chiral 3D hybrid organic–inorganic perovskites, Adv. Mater. 31 (2019), 1807628.

[54] L. He, P.-P. Shi, L. Zhou, Z.-B. Liu, W. Zhang, Q. Ye, Coexisting ferroelectric and ferroelastic orders in rare 3D homochiral hybrid bimetal halides, Chem. Mater. 33 (2021) 6233–6239.

[55] H. Lin, C. Zhou, Y. Tian, T. Siegrist, B. Ma, Low-dimensional organometal halide perovskites, ACS Energy Lett. 3 (2018) 54–62.

[56] P. Chen, Y. Bai, M. Lyu, J.-H. Yun, M. Hao, L. Wang, Progress and perspective in low-dimensional metal halide perovskites for optoelectronic applications, Sol. RRL 2 (2018), 1700186.

[57] C.-K. Yang, W.-N. Chen, Y.-T. Ding, J. Wang, Y. Rao, W.-Q. Liao, Y.-Y. Tang, P.-F. Li, Z.-X. Wang, R.-G. Xiong, The first 2D homochiral lead iodide perovskite ferroelectrics: [R- and S-1-(4-chlorophenyl)ethylammonium]$_2$PbI$_4$, Adv. Mater. 31 (2019), 1808088.

[58] F. Zhang, H. Lu, J. Tong, J.J. Berry, M.C. Beard, K. Zhu, Advances in two-dimensional organic–inorganic hybrid perovskites, Energy Environ. Sci. 13 (2020) 1154–1186.

[59] F. Thouin, D.A. Valverde-Chávez, C. Quarti, D. Cortecchia, I. Bargigia, D. Beljonne, A. Petrozza, C. Silva, A.R. Srimath Kandada, Phonon coherences reveal the polaronic character of excitons in two-dimensional lead halide perovskites, Nat. Mater. 18 (2019) 349–356.

[60] G. Long, C. Jiang, R. Sabatini, Z. Yang, M. Wei, LN. Quan, Q. Liang, A. Rasmita, M. Askerka, G. Walters, X. Gong, J. Xing, X. Wen, R. Quintero-Bermudez, H. Yuan, G. Xing, X.R. Wang, D. Song, O. Voznyy, M. Zhang, S. Hoogland, W. Gao, Q. Xiong, E.H. Sargent, Spin control in reduced-dimensional chiral perovskites, Nat. Photonics 12 (2018) 528–533.

[61] L. Wang, Y. Xue, M. Cui, Y. Huang, H. Xu, C. Qin, J. Yang, H. Dai, M. Yuan, A chiral reduced-dimension perovskite for an efficient flexible circularly polarized light photodetector, Angew. Chem. Int. Ed. 59 (2020) 6442–6450.

[62] C. Chen, L. Gao, W. Gao, C. Ge, X. Du, Z. Li, Y. Yang, G. Niu, J. Tang, Circularly polarized light detection using chiral hybrid perovskite, Nat. Commun. 10 (2019) 1927.

[63] Y. Peng, Y. Yao, L. Li, Z. Wu, S. Wang, J. Luo, White-light emission in a chiral one-dimensional organic–inorganic hybrid perovskite, J. Mater. Chem. C 6 (2018) 6033–6037.

[64] Z. Guo, J. Li, C. Wang, R. Liu, J. Liang, Y. Gao, J. Cheng, W. Zhang, X. Zhu, R. Pan, T. He, Giant optical activity and second harmonic generation in 2D hybrid copper halides, Angew. Chem. Int. Ed. 60 (2021) 8441–8445.

[65] L. Yao, G. Niu, J. Li, L. Gao, X. Luo, B. Xia, Y. Liu, P. Du, D. Li, C. Chen, Y. Zheng, Z. Xiao, J. Tang, Circularly polarized luminescence from chiral tetranuclear copper(I) iodide clusters, J. Phys. Chem. Lett. 11 (2020) 1255–1260.

[66] L.-S. Li, Y.-H. Tan, W.-J. Wei, H.-Q. Gao, Y.-Z. Tang, X.-B. Han, Chiral switchable low-dimensional perovskite ferroelectrics, ACS Appl. Mater. Interfaces 13 (2021) 2044–2051.

[67] J. Webb, R.W. Strickland, F.S. Richardson, Optical activity of chiral disulfide chromophores, J. Am. Chem. Soc. 95 (1973) 4775–4783.

[68] N. Mercier, A.-L. Barres, M. Giffard, I. Rau, F. Kajzar, B. Sahraoui, Conglomerate-to-true-racemate reversible solid-state transition in crystals of an organic disulfide-based iodoplumbate, Angew. Chem. Int. Ed. 45 (2006) 2100–2103.

[69] W. Bi, N. Louvain, N. Mercier, J. Luc, I. Rau, F. Kajzar, B. Sahraoui, A switchable NLO organic-inorganic compound based on conformationally chiral disulfide molecules and Bi(III)I$_5$ iodobismuthate networks, Adv. Mater. 20 (2008) 1013–1017.

[70] H.-R. Zhao, D.-P. Li, X.-M. Ren, Y. Song, W.-Q. Jin, Larger spontaneous polarization ferroelectric inorganic–organic hybrids: [PbI$_3$]$_\infty$ chains directed organic cations aggregation to Kagomé-shaped tubular architecture, J. Am. Chem. Soc. 132 (2010) 18–19.

[71] A. Ishii, T. Miyasaka, Direct detection of circular polarized light in helical 1D perovskite-based photodiode, Sci. Adv. 6 (2020), eabd3274.

[72] Q.H. Wang, K. Kalantar-Zadeh, A. Kis, J.N. Coleman, M.S. Strano, Electronics and optoelectronics of two-dimensional transition metal dichalcogenides, Nat. Nanotechnol. 7 (2012) 699–712.

[73] S. Manzeli, D. Ovchinnikov, D. Pasquier, O.V. Yazyev, A. Kis, 2D transition metal dichalcogenides, Nat. Rev. Mater. 2 (2017), 17033.

[74] Z. Zhang, S. Wang, X. Liu, Y. Chen, C. Su, Z. Tang, Y. Li, G. Xing, Metal halide perovskite/2D material heterostructures: syntheses and applications, Small Methods 5 (2021), 2000937.

[75] Y. Chen, Z. Liu, J. Li, X. Cheng, J. Ma, H. Wang, D. Li, Robust interlayer coupling in two-dimensional perovskite/monolayer transition metal dichalcogenide heterostructures, ACS Nano 14 (2020) 10258–10264.

[76] Y. Chen, J. Ma, Z. Liu, J. Li, X. Duan, D. Li, Manipulation of valley pseudospin by selective spin injection in chiral two-dimensional perovskite/monolayer transition metal dichalcogenide heterostructures, ACS Nano 14 (2020) 15154–15160.

[77] X. Zhang, X. Liu, L. Li, C. Ji, Y. Yao, J. Luo, Great amplification of circular polarization sensitivity via heterostructure engineering of a chiral two-dimensional hybrid perovskite crystal with a three-dimensional MAPbI$_3$ crystal, ACS Cent. Sci. 143 (2021) 8437–8445.

[78] A. Lemmerer, D. Billings, Inorganic–organic hybrids incorporating a chiral cyclic ammonium cation, S. Afr. J. Chem. 66 (2013) 263–272.

[79] A.M. Ben Salah, N. Sayari, H. Naïli, A.J. Norquist, Chiral and achiral copper(II) complexes: structure, bonding and biological activities, RSC Adv. 6 (2016) 59055–59065.

[80] P.-J. Huang, K. Taniguchi, H. Miyasaka, Bulk photovoltaic effect in a pair of chiral–polar layered perovskite-type lead iodides altered by chirality of organic cations, J. Am. Chem. Soc. 141 (2019) 14520–14523.

[81] H. Lu, J. Wang, C. Xiao, X. Pan, X. Chen, R. Brunecky, J.J. Berry, K. Zhu, M.C. Beard, Z.V. Vardeny, Spin-dependent charge transport through 2D chiral hybrid lead-iodide perovskites, Sci. Adv. 5 (2019), eaay0571.

[82] J. Ma, C. Fang, C. Chen, L. Jin, J. Wang, S. Wang, J. Tang, D. Li, Chiral 2D perovskites with a high degree of circularly polarized photoluminescence, ACS Nano 13 (2019) 3659–3665.

[83] Y. Peng, Y. Yao, L. Li, X. Liu, X. Zhang, Z. Wu, S. Wang, C. Ji, W. Zhang, J. Luo, Exploration of chiral organic–inorganic hybrid semiconducting lead halides, Chem. Asian J. 14 (2019) 2273–2277.

[84] Y. Dang, X. Liu, Y. Sun, J. Song, W. Hu, X. Tao, Bulk chiral halide perovskite single crystals for active circular dichroism and circularly polarized luminescence, J. Phys. Chem. Lett. 11 (2020) 1689–1696.

[85] N. Dehnhardt, M. Axt, J. Zimmermann, M. Yang, G. Mette, J. Heine, Band gap-tunable, chiral hybrid metal halides displaying second-harmonic generation, Chem. Mater. 32 (2020) 4801–4807.

[86] Y. Hu, F. Florio, Z. Chen, W.A. Phelan, M.A. Siegler, Z. Zhou, Y. Guo, R. Hawks, J. Jiang, J. Feng, L. Zhang, B. Wang, Y. Wang, D. Gall, E.F. Palermo, Z. Lu, X. Sun, T.-M. Lu, H. Zhou, Y. Ren, E. Wertz, R. Sundararaman, J. Shi, A chiral switchable photovoltaic ferroelectric 1D perovskite, Sci. Adv. 6 (2020), eaay4213.

[87] Z. Huang, B.P. Bloom, X. Ni, Z.N. Georgieva, M. Marciesky, E. Vetter, F. Liu, D.H. Waldeck, D. Sun, Magneto-optical detection of photoinduced magnetism via chirality-induced spin selectivity in 2D chiral hybrid organic–inorganic perovskites, ACS Nano 14 (2020) 10370–10375.

[88] D. Li, X. Liu, W. Wu, Y. Peng, S. Zhao, L. Li, M. Hong, J. Luo, Chiral lead-free hybrid perovskites for self-powered circularly polarized light detection, Angew. Chem. Int. Ed. 60 (2021) 8415–8418.

[89] Y. Li, T. Yang, X. Liu, S. Han, J. Wang, Y. Ma, W. Guo, J. Luo, Z. Sun, A chiral lead-free photoactive hybrid material with a narrow bandgap, Inorg. Chem. Front. 7 (2020) 2770–2777.

[90] Y. Liu, C. Wang, Y. Guo, L. Ma, C. Zhou, Y. Liu, L. Zhu, X. Li, M. Zhang, G. Zhao, New lead bromide chiral perovskites with ultra-broadband white-light emission, J. Mater. Chem. C 8 (2020) 5673–5680.

[91] B. Sun, X.-F. Liu, X.-Y. Li, Y. Zhang, X. Shao, D. Yang, H.-L. Zhang, Two-dimensional perovskite chiral ferromagnets, Chem. Mater. 32 (2020) 8914–8920.

[92] C. Zhou, Y. Chu, L. Ma, Y. Zhong, C. Wang, Y. Liu, H. Zhang, B. Wang, X. Feng, X. Yu, X. Zhang, Y. Sun, X. Li, G. Zhao, Photoluminescence spectral broadening, chirality transfer and amplification of chiral perovskite materials (R-X-p-mBZA)$_2$PbBr$_4$ (X = H, F, Cl, Br) regulated by van der Waals and halogen atoms interactions, Phys. Chem. Chem. Phys. 22 (2020) 17299–17305.

[93] J. Hao, H. Lu, L. Mao, X. Chen, M.C. Beard, J.L. Blackburn, Direct detection of circularly polarized light using chiral copper chloride–carbon nanotube heterostructures, ACS Nano 15 (2021) 7608–7617.

[94] P.-J. Huang, K. Taniguchi, M. Shigefuji, T. Kobayashi, M. Matsubara, T. Sasagawa, H. Sato, H. Miyasaka, Chirality-dependent circular photogalvanic effect in enantiomorphic 2D organic–inorganic hybrid perovskites, Adv. Mater. 33 (2021), 2008611.

[95] A. Singh, M.K. Jana, D.B. Mitzi, Reversible crystal–glass transition in a metal halide perovskite, Adv. Mater. 33 (2021), 2005868.

[96] J. Wang, H. Lu, X. Pan, J. Xu, H. Liu, X. Liu, D.R. Khanal, M.F. Toney, M.C. Beard, Z.V. Vardeny, Spin-dependent photovoltaic and photogalvanic responses of optoelectronic devices based on chiral two-dimensional hybrid organic–inorganic perovskites, ACS Nano 15 (2021) 588–595.

[97] Y.-L. Zeng, X.-Q. Huang, C.-R. Huang, H. Zhang, F. Wang, Z.-X. Wang, Unprecedented 2D homochiral hybrid lead-iodide perovskite thermochromic ferroelectrics with ferroelastic switching, Angew. Chem. Int. Ed. 60 (2021) 10730–10735.

[98] J.-T. Lin, D.-G. Chen, L.-S. Yang, T.-C. Lin, Y.-H. Liu, Y.-C. Chao, P.-T. Chou, C.-W. Chiu, Tuning the circular dichroism and circular polarized luminescence intensities of chiral 2D hybrid organic-inorganic perovskites through halogenation of the organic ions, Angew. Chem. Int. Ed. 60 (2021) 21434–21440.

[99] Y. Lu, Q. Wang, R. Chen, L. Qiao, F. Zhou, X. Yang, J. Wang, D. Wang, H. Cao, W. He, F. Pan, Z. Yang, C. Song, Spin-dependent charge transport in 1D chiral hybrid lead-bromide perovskite with high stability, Adv. Funct. Mater. 31 (2021), 2104605.

[100] Y. Peng, X. Liu, L. Li, Y. Yao, H. Ye, X. Shang, X. Chen, J. Luo, Realization of vis–NIR dual-modal circularly polarized light detection in chiral perovskite bulk crystals, J. Am. Chem. Soc. 143 (2021) 14077–14082.

[101] D. Fu, J. Xin, Y. He, S. Wu, X. Zhang, X.-M. Zhang, J. Luo, Chirality-dependent second-order nonlinear optical effects in 1D organic-inorganic hybrid perovskites bulk single crystal, Angew. Chem. Int. Ed. 60 (2021) 20021–20026.

[102] J. Ma, C. Fang, L. Liang, H. Wang, D. Li, Full-Stokes polarimeter based on chiral perovskites with chirality and large optical anisotropy, Small 17 (2021), 2103855.

[103] L. Yao, Z. Zeng, C. Cai, P. Xu, H. Gu, L. Gao, J. Han, X. Zhang, X. Wang, X. Wang, A. Pan, J. Wang, W. Liang, S. Liu, C. Chen, J. Tang, Strong second- and third-harmonic generation in 1D chiral hybrid bismuth halides, J. Am. Chem. Soc. 143 (2021) 16095–16104.

[104] Z. Zhang, Y. Lin, J. Jin, L. Gong, Y. Peng, Y. Song, N. Shen, Z. Wang, K. Du, X. Huang, Crystalline-phase-recognition-induced domino phase transition and luminescence switching for advanced information encryption, Angew. Chem. Int. Ed. 60 (2021) 23373–23379.

[105] Y. Zheng, J. Xu, X.-H. Bu, 1D Chiral lead halide perovskites with superior second-order optical nonlinearity, Adv. Opt. Mater. 10 (2022), 2101545.

[106] L. Yan, M.K. Jana, P.C. Sercel, D.B. Mitzi, W. You, Alkyl–aryl cation mixing in chiral 2D perovskites, J. Am. Chem. Soc. 143 (2021) 18114–18120.

[107] R.S. Black, D.G. Billing, The structure and photoluminescence of chiral tin and lead inorganic-organic hybrid perovskites, Acta Crystallogr. A64 (2008) C455–C456.

[108] H.M. Mande, P.S. Ghalsasi, N. Arulsamy, Racemic and conglomerate 1-(4-haloaryl)ethylammonium tetrachlorocobaltate salts: formation of helical structures, RSC Adv. 5 (2015) 62719–62723.

[109] H.M. Mande, P.S. Ghalsasi, A. Navamoney, Synthesis, structural and spectroscopic characterization of the thermochromic compounds A$_2$CuCl$_4$: [(naphthyl ethylammonium)$_2$CuCl$_4$], Polyhedron 91 (2015) 141–149.

[110] T.H. Moon, S.-J. Oh, K.M. Ok, [((R)-C$_8$H$_{12}$N)$_4$][Bi$_2$Br$_{10}$] and [((S)-C$_8$H$_{12}$N)$_4$][Bi$_2$Br$_{10}$]: chiral hybrid bismuth bromides templated by chiral organic cations, ACS Omega 3 (2018) 17895–17903.

[111] Y. Ai, X.-G. Chen, P.-P. Shi, Y.-Y. Tang, P.-F. Li, W.-Q. Liao, R.-G. Xiong, Fluorine substitution induced high T$_c$ of enantiomeric perovskite ferroelectrics: (R)- and (S)-3-(fluoropyrrolidinium)MnCl$_3$, J. Am. Chem. Soc. 141 (2019) 4474–4479.

[112] F. Hajlaoui, I.B. Hadj Sadok, H.A. Aeshah, N. Audebrand, T. Roisnel, N. Zouari, Synthesis, crystal structures, second harmonic generation response and temperature phase transitions of two noncentrosymmetric Cu(II)-hybrid halides compounds: [(R)-C$_7$H$_{16}$N$_2$][CuX$_4$] (X = Cl or Br), J. Mol. Struct. 1182 (2019) 47–53.

[113] W.-H. Hu, W.-J. Xu, Q.-R. Meng, X.-W. Zhang, C.-T. He, W.-X. Zhang, X.-M. Chen, Switching hydrogen bonds to readily interconvert two room-temperature long-term stable crystalline polymorphs in chiral molecular perovskites, Chem. Commun. 55 (2019) 11555–11558.

[114] Y.-Y. Tang, Y. Ai, W.-Q. Liao, P.-F. Li, Z.-X. Wang, R.-G. Xiong, H/F-substitution-induced homochirality for designing high-T$_c$ molecular perovskite ferroelectrics, Adv. Mater. 31 (2019), 1902163.

[115] J. Zhao, T. Zhang, X.-Y. Dong, M.-E. Sun, C. Zhang, X. Li, Y.S. Zhao, S.-Q. Zang, Circularly polarized luminescence from achiral single crystals of hybrid manganese halides, J. Am. Chem. Soc. 141 (2019) 15755–15760.

[116] L.-L. Zhu, Y.-E. Huang, Y.-P. Lin, X.-Y. Huang, H.-Q. Liu, D.B. Mitzi, K.-Z. Du, Stereochemically active lead chloride enantiomers mediated by homochiral organic cation, Polyhedron 158 (2019) 445–448.

[117] J.-X. Gao, W.-Y. Zhang, Z.-G. Wu, Y.-X. Zheng, D.-W. Fu, Enantiomorphic perovskite ferroelectrics with circularly polarized luminescence, J. Am. Chem. Soc. 142 (2020) 4756–4761.

[118] M. Takahashi, N. Hoshino, K. Sambe, T. Takeda, T. Akutagawa, Dynamics of chiral cations in two-dimensional CuX$_4$ and PbX$_4$ perovskites (X = Cl and Br), Inorg. Chem. 59 (2020) 11606–11615.

[119] K. Trujillo-Hernández, G. Rodríguez-López, A. Espinosa-Roa, J. González-Roque, A.P. Gómora-Figueroa, W. Zhang, P.S. Halasyamani, V. Jancik, M. Gembicky, G. Pirruccio, D. Solis-Ibarra, Chirality control in white-light emitting 2D perovskites, J. Mater. Chem. C 8 (2020) 9602–9607.

[120] H. Peng, H. Cheng, Y.-H. Liu, M.-J. Yang, W.-Q. Liao, Y. Ai, Enantiomeric perovskite with a dual phase transition at high temperature, J. Mater. Chem. C 9 (2021) 1918–1922.

[121] H. Ye, W.-H. Hu, W.-J. Xu, Y. Zeng, X.-X. Chen, R.-K. Huang, W.-X. Zhang, X.-M. Chen, Two enantiomeric perovskite ferroelectrics with a high T$_c$ raised by inserting intermolecular hydrogen bonds, Apl. Mater. 9 (2021), 031102.

[122] H. Peng, Y.-H. Liu, X.-Q. Huang, Q. Liu, Z.-H. Yu, Z.-X. Wang, W.-Q. Liao, Homochiral one-dimensional ABX$_3$ lead halide perovskites with high-T$_c$ quadratic nonlinear optical and dielectric switchings, Mater. Chem. Front. 5 (2021) 4756–4763.

[123] R.-G. Xiong, S.-Q. Lu, Z.-X. Zhang, H. Cheng, P.-F. Li, W.-Q. Liao, A chiral thermochromic ferroelastic with seven physical channel switches, Angew. Chem. Int. Ed. 59 (2020) 9574–9578.

[124] H.-Y. Shen, L. He, P.-P. Shi, Q. Ye, Lead-free organic–inorganic hybrid semiconductors and NLO switches tuned by dimensional design, J. Mater. Chem. C 9 (2021) 4338–4343.

[125] F.-F. Gao, X. Li, Y. Qin, Z.-G. Li, T.-M. Guo, Z.-Z. Zhang, G.-D. Su, C. Jiang, M. Azeem, W. Li, X. Wu, X.-H. Bu, Dual-stimuli-responsive photoluminescence of enantiomeric two-dimensional lead halide perovskites, Adv. Opt. Mater. 9 (2021), 2100003.

[126] K. Taniguchi, M. Nishio, N. Abe, P.-J. Huang, S. Kimura, T.-h. Arima, H. Miyasaka, Magneto-electric directional anisotropy in polar soft ferromagnets of two-dimensional organic-inorganic hybrid perovskites, Angew. Chem. Int. Ed. 60 (2021) 14350–14354.

[127] L. Zhao, X. Han, Y. Zheng, M.-H. Yu, J. Xu, Tin-based chiral perovskites with second-order nonlinear optical properties, Adv. Photonics Res. 2 (2021), 2100056.

[128] Y. Lu, Q. Wang, R. He, F. Zhou, X. Yang, D. Wang, H. Cao, W. He, F. Pan, Z. Yang, C. Song, Highly-efficient spin-filtering transport in chiral hybrid copper halides, Angew. Chem. Int. Ed. 60 (2021) 23578–23583.

[129] V.Y. Sirenko, O.I. Kucheriv, D.D. Naumova, I. Fesich, R. Linnik, A. Dascalu, S. Shova, I.O. Fritsky, I.y.A. Gural'skiy, Chiral organic-inorganic lead halide perovskites based on α-alanine, New J. Chem. 45 (2021) 12606–12612.

[130] C. Yuan, X. Li, S. Semin, Y. Feng, T. Rasing, J. Xu, Chiral lead halide perovskite nanowires for second-order nonlinear optics, Nano Lett. 18 (2018) 5411–5417.

[131] J. Wang, C. Fang, J. Ma, S. Wang, L. Jin, W. Li, D. Li, Aqueous synthesis of low-dimensional lead halide perovskites for room-temperature circularly polarized light emission and detection, ACS Nano 13 (2019) 9473–9481.

[132] Y. Dang, Y. Liu, Y. Sun, D. Yuan, X. Liu, W. Lu, G. Liu, H. Xia, X. Tao, Bulk crystal growth of hybrid perovskite material CH$_3$NH$_3$PbI$_3$, CrystEngComm 17 (2015) 665–670.

[133] Z. Guo, J. Li, R. Pan, J. Cheng, R. Chen, T. He, All-inorganic copper(I)-based ternary metal halides: promising materials toward optoelectronics, Nanoscale 12 (2020) 15560–15576.

[134] R. Babu, L. Giribabu, S.P. Singh, Recent advances in halide-based perovskite crystals and their optoelectronic applications, Cryst. Growth Des. 18 (2018) 2645–2664.

[135] Y. Liu, Z. Yang, S. Liu, Recent progress in single-crystalline perovskite research including crystal preparation, property evaluation, and applications, Adv. Sci. 5 (2018), 1700471.

[136] C.C. Stoumpos, D.H. Cao, D.J. Clark, J. Young, J.M. Rondinelli, J.I. Jang, J.T. Hupp, M.G. Kanatzidis, Ruddlesden–popper hybrid lead iodide perovskite 2D homologous semiconductors, Chem. Mater. 28 (2016) 2852–2867.

[137] R. Hulst, N.K. de Vries, B.L. Feringa, α-Phenylethylamine based chiral phospholidines; new agents for the determination of the enantiomeric excess of chiral alcohols, amines and thiols by means of ^{31}P NMR, Tetrahedron Asymmetry 5 (1994) 699–708.

[138] C. Geng, S. Xu, H. Zhong, A.L. Rogach, W. Bi, Aqueous synthesis of methylammonium lead halide perovskite nanocrystals, Angew. Chem. Int. Ed. 57 (2018) 9650–9654.

[139] X. Zhang, R. Munir, Z. Xu, Y. Liu, H. Tsai, W. Nie, J. Li, T. Niu, D.-M. Smilgies, M.G. Kanatzidis, A.D. Mohite, K. Zhao, A. Amassian, S. Liu, Phase transition control for high performance ruddlesden–popper perovskite solar cells, Adv. Mater. 30 (2018), 1707166.

[140] R. Quintero-Bermudez, A. Gold-Parker, A.H. Proppe, R. Munir, Z. Yang, S.O. Kelley, A. Amassian, M.F. Toney, E.H. Sargent, Compositional and orientational control in metal halide perovskites of reduced dimensionality, Nat. Mater. 17 (2018) 900–907.

[141] J.A. Schellman, Circular dichroism and optical rotation, Chem. Rev. 75 (1975) 323–331.

[142] J.P. Riehl, F.S. Richardson, Circularly polarized luminescence spectroscopy, Chem. Rev. 86 (1986) 1–16.

[143] S.M. Kelly, T.J. Jess, N.C. Price, How to study proteins by circular dichroism, Biochim. Biophys. Acta 1751 (2005) 119–139.

[144] A. Rodger, B. Nordén, Circular Dichroism and Linear Dichroism, Oxford University Press, USA, 1997.

[145] F. Zinna, L. Di Bari, Lanthanide circularly polarized luminescence: bases and applications, Chirality 27 (2015) 1–13.

[146] N. Berova, K. Nakanishi, R.W. Woody, Circular Dichroism: Principles and Applications, John Wiley & Sons, 2000.

[147] A.O. Govorov, Z. Fan, P. Hernandez, J.M. Slocik, R.R. Naik, Theory of circular dichroism of nanomaterials comprising chiral molecules and nanocrystals: plasmon enhancement, dipole interactions, and dielectric effects, Nano Lett. 10 (2010) 1374–1382.

[148] W. Ma, L. Xu, A.F. de Moura, X. Wu, H. Kuang, C. Xu, N.A. Kotov, Chiral inorganic nanostructures, Chem. Rev. 117 (2017) 8041–8093.

[149] H. Tanaka, Y. Inoue, T. Mori, Circularly polarized luminescence and circular dichroisms in small organic molecules: correlation between excitation and emission dissymmetry factors, ChemPhotoChem 2 (2018) 386–402.

[150] Z. Xiao, W. Meng, J. Wang, D.B. Mitzi, Y. Yan, Searching for promising new perovskite-based photovoltaic absorbers: the importance of electronic dimensionality, Mater. Horiz. 4 (2017) 206–216.

[151] A. Goyal, S. McKechnie, D. Pashov, W. Tumas, M. van Schilfgaarde, V. Stevanović, Origin of pronounced nonlinear band gap behavior in lead–tin hybrid perovskite alloys, Chem. Mater. 30 (2018) 3920–3928.

[152] Z.-G. Wu, H.-B. Han, Z.-P. Yan, X.-F. Luo, Y. Wang, Y.-X. Zheng, J.-L. Zuo, Y. Pan, Chiral octahydro-binaphthol compound-based thermally activated delayed fluorescence materials for circularly polarized electroluminescence with superior EQE of 32.6% and extremely low efficiency roll-off, Adv. Mater. 31 (2019), 1900524.

[153] D.-W. Zhang, M. Li, C.-F. Chen, Recent advances in circularly polarized electroluminescence based on organic light-emitting diodes, Chem. Soc. Rev. 49 (2020) 1331–1343.

[154] T. Han, S. Zu, Z. Li, M. Jiang, X. Zhu, Z. Fang, Reveal and control of chiral cathodoluminescence at subnanoscale, Nano Lett. 18 (2018) 567–572.

[155] V. Sharma, M. Crne, O. Park Jung, M. Srinivasarao, Structural origin of circularly polarized iridescence in jeweled beetles, Science 325 (2009) 449–451.

[156] R. Farshchi, M. Ramsteiner, J. Herfort, A. Tahraoui, H.T. Grahn, Optical communication of spin information between light emitting diodes, Appl. Phys. Lett. 98 (2011), 162508.
[157] Yakir L. Gagnon, Rachel M. Templin, Martin J. How, N.J. Marshall, Circularly polarized light as a communication signal in mantis shrimps, Curr. Biol. 25 (2015) 3074–3078.
[158] P.C. Sercel, Z.V. Vardeny, A.L. Efros, Circular dichroism in non-chiral metal halide perovskites, Nanoscale 12 (2020) 18067–18078.
[159] J.K. O'Loane, Optical activity in small molecules, nonenantiomorphous crystals, and nematic liquid crystals, Chem. Rev. 80 (1980) 41–61.
[160] R. Gautier, J.M. Klingsporn, R.P. Van Duyne, K.R. Poeppelmeier, Optical activity from racemates, Nat. Mater. 15 (2016) 591–592.
[161] Z. Wang, M. Gao, X. Hao, W. Qin, Helical-chiroptical nanowires generated orbital angular momentum for the detection of circularly polarized light, Appl. Phys. Lett. 116 (2020), 053301.
[162] Y. Yang, R.C. da Costa, M.J. Fuchter, A.J. Campbell, Circularly polarized light detection by a chiral organic semiconductor transistor, Nat. Photonics 7 (2013) 634–638.
[163] W. Li, Z.J. Coppens, L.V. Besteiro, W. Wang, A.O. Govorov, J. Valentine, Circularly polarized light detection with hot electrons in chiral plasmonic metamaterials, Nat. Commun. 6 (2015) 8379.
[164] X. Zhang, W. Weng, L. Li, H. Wu, Y. Yao, Z. Wang, X. Liu, W. Lin, J. Luo, Heterogeneous integration of chiral lead–chloride perovskite crystals with Si wafer for boosted circularly polarized light detection in solar-blind ultraviolet region, Small 17 (2021), 2102884.
[165] Y. Zhao, Y. Qiu, J. Feng, J. Zhao, G. Chen, H. Gao, Y. Zhao, L. Jiang, Y. Wu, Chiral 2D-perovskite nanowires for Stokes photodetectors, J. Am. Chem. Soc. 143 (2021) 8437–8445.
[166] Z. Liu, C. Zhang, X. Liu, A. Ren, Z. Zhou, C. Qiao, Y. Guan, Y. Fan, F. Hu, Y.S. Zhao, Chiral hybrid perovskite single-crystal nanowire arrays for high-performance circularly polarized light detection, Adv. Sci. 8 (2021), 2102065.
[167] W. Shockley, H.J. Queisser, Detailed balance limit of efficiency of p-n junction solar cells, J. Appl. Phys. 32 (1961) 510–519.
[168] L.Z. Tan, F. Zheng, S.M. Young, F. Wang, S. Liu, A.M. Rappe, Shift current bulk photovoltaic effect in polar materials—hybrid and oxide perovskites and beyond, NPJ Comput. Mater. 2 (2016), 16026.
[169] A. Zenkevich, Y. Matveyev, K. Maksimova, R. Gaynutdinov, A. Tolstikhina, V. Fridkin, Giant bulk photovoltaic effect in thin ferroelectric BaTiO$_3$ films, Phys. Rev. B 90 (2014), 161409.
[170] B.A. Connor, L. Leppert, M.D. Smith, J.B. Neaton, H.I. Karunadasa, Layered halide double perovskites: dimensional reduction of Cs$_2$AgBiBr$_6$, J. Am. Chem. Soc. 140 (2018) 5235–5240.
[171] J.F. Scott, Applications of modern ferroelectrics, Science 315 (2007) 954.
[172] W. Zhang, R.-G. Xiong, Ferroelectric metal–organic frameworks, Chem. Rev. 112 (2012) 1163–1195.
[173] S. Shahrokhi, W. Gao, Y. Wang, P.R. Anandan, M.Z. Rahaman, S. Singh, D. Wang, C. Cazorla, G. Yuan, J.-M. Liu, T. Wu, Emergence of ferroelectricity in halide perovskites, Small Methods 4 (2020), 2000149.
[174] P.-P. Shi, Y.-Y. Tang, P.-F. Li, W.-Q. Liao, Z.-X. Wang, Q. Ye, R.-G. Xiong, Symmetry breaking in molecular ferroelectrics, Chem. Soc. Rev. 45 (2016) 3811–3827.
[175] L. Sui Li, W. Juan Wei, H. Qiang Gao, Y. Hui Tan, X. Bo Han, Molecular disorder induces an unusual phase transition in a potential 2D chiral ferroelectric perovskite, Chem. Eur J. 27 (2021) 9054–9059.
[176] H.-Y. Liu, H.-Y. Zhang, X.-G. Chen, R.-G. Xiong, Molecular design principles for ferroelectrics: ferroelectrochemistry, J. Am. Chem. Soc. 142 (2020) 15205–15218.
[177] W.-J. Xu, C.-T. He, C.-M. Ji, S.-L. Chen, R.-K. Huang, R.-B. Lin, W. Xue, J.-H. Luo, W.-X. Zhang, X.-M. Chen, Molecular dynamics of flexible polar cations in a variable confined space: toward exceptional two-step nonlinear optical switches, Adv. Mater. 28 (2016) 5886–5890.
[178] Y. Zhang, W.-Q. Liao, D.-W. Fu, H.-Y. Ye, Z.-N. Chen, R.-G. Xiong, Highly efficient red-light emission in an organic–inorganic hybrid ferroelectric: (pyrrolidinium)MnCl$_3$, J. Am. Chem. Soc. 137 (2015) 4928–4931.
[179] K. Ray, S.P. Ananthavel, D.H. Waldeck, R. Naaman, Asymmetric scattering of polarized electrons by organized organic films of chiral molecules, Science 283 (1999) 814.
[180] R. Naaman, D.H. Waldeck, Chiral-induced spin selectivity effect, J. Phys. Chem. Lett. 3 (2012) 2178–2187.
[181] R. Naaman, D.H. Waldeck, Spintronics and chirality: spin selectivity in electron transport through chiral molecules, Annu. Rev. Phys. Chem. 66 (2015) 263–281.
[182] R. Naaman, Y. Paltiel, D.H. Waldeck, Chiral molecules and the electron spin, Nat. Rev. Chem. 3 (2019) 250–260.
[183] S.-H. Yang, R. Naaman, Y. Paltiel, S.S.P. Parkin, Chiral spintronics, Nat. Rev. Phys. 3 (2021) 328–343.
[184] Z.-G. Yu, Chirality-induced spin–orbit coupling, spin transport, and natural optical activity in hybrid organic–inorganic perovskites, J. Phys. Chem. Lett. 11 (2020) 8638–8646.
[185] A. Soumyanarayanan, N. Reyren, A. Fert, C. Panagopoulos, Emergent phenomena induced by spin–orbit coupling at surfaces and interfaces, Nature 539 (2016) 509–517.
[186] E.I. Rashba, Properties of semiconductors with an extremum loop. I. Cyclotron and combinational resonance in a magnetic field perpendicular to the plane of the loop, Sov. Phys. Solid State 2 (1960) 1109–1122.
[187] G. Dresselhaus, Spin-orbit coupling effects in zinc blende structures, Phys. Rev. 100 (1955) 580–586.
[188] M. Kepenekian, R. Robles, C. Katan, D. Sapori, L. Pedesseau, J. Even, Rashba and dresselhaus effects in hybrid organic–inorganic perovskites: from basics to devices, ACS Nano 9 (2015) 11557–11567.
[189] C. Zhang, D. Sun, C.X. Sheng, Y.X. Zhai, K. Mielczarek, A. Zakhidov, Z.V. Vardeny, Magnetic field effects in hybrid perovskite devices, Nat. Phys. 11 (2015) 427–434.
[190] L.E. Golub, Spin-splitting-induced photogalvanic effect in quantum wells, Phys. Rev. B 67 (2003), 235320.
[191] J.W. McIver, D. Hsieh, H. Steinberg, P. Jarillo-Herrero, N. Gedik, Control over topological insulator photocurrents with light polarization, Nat. Nanotechnol. 7 (2012) 96–100.
[192] Y. Zhou, Y. Huang, X. Xu, Z. Fan, J.B. Khurgin, Q. Xiong, Nonlinear optical properties of halide perovskites and their applications, Appl. Phys. Rev. 7 (2020), 041313.
[193] J. Xu, X. Li, J. Xiong, C. Yuan, S. Semin, T. Rasing, X.-H. Bu, Halide perovskites for nonlinear optics, Adv. Mater. 32 (2020), 1806736.
[194] W. Chen, F. Zhang, C. Wang, M. Jia, X. Zhao, Z. Liu, Y. Ge, Y. Zhang, H. Zhang, Nonlinear photonics using low-dimensional metal-halide perovskites: recent advances and future challenges, Adv. Mater. 33 (2021), 2004446.
[195] W. Shen, J. Chen, J. Wu, X. Li, H. Zeng, Nonlinear optics in lead halide perovskites: mechanisms and applications, ACS Photonics 8 (2021) 113–124.
[196] Y.R. Shen, The Principles of Nonlinear Optics, John Wiley & Sons, New York, 1984.
[197] S. Govinda, B.P. Kore, P. Mahale, A. Pandey, D.D. Sarma, Can SHG measurements determine the polarity of hybrid lead halide perovskites? ACS Energy Lett. 3 (2018) 1887–1891.
[198] J. Zhao, Y. Zhao, Y. Guo, X. Zhan, J. Feng, Y. Geng, X. Yuan, M. Fan, H. Gao, L. Jiang, Y. Yan, Y. Wu, Layered metal-halide perovskite single-crystalline microwire arrays for anisotropic nonlinear optics, Adv. Funct. Mater. 31 (2021), 2105855.
[199] H. Ren, Y. Wu, C. Wang, Y. Yan, 2D perovskite nanosheets with intrinsic chirality, J. Phys. Chem. Lett. 12 (2021) 2676–2681.
[200] Z. Chen, G. Dong, J. Qiu, Ultrafast pump-probe spectroscopy—a powerful tool for tracking spin-quantum dynamics in metal halide perovskites, Adv. Quantum Technol. 4 (2021), 2100052.
[201] W. Zhao, R. Su, Y. Huang, J. Wu, C.F. Fong, J. Feng, Q. Xiong, Transient circular dichroism and exciton spin dynamics in all-inorganic halide perovskites, Nat. Commun. 11 (2020) 5665.